6-2009

A Microresonator Design Based on Nonlinear 1:2 Internal Resonance in Flexural Structural Modes

Ashwin Vyas
Purdue University - Main Campus, ashwinv@purdue.edu

Dimitrios Peroulis
Birck Nanotechnology Center, Purdue University, dperouli@purdue.edu

Anil Bajaj
Purdue University - Main Campus, anil.k.bajaj.1@purdue.edu

A Microresonator Design Based on Nonlinear 1 : 2 Internal Resonance in Flexural Structural Modes

Ashwin Vyas, *Student Member, ASME*, Dimitrios Peroulis, *Member, IEEE*, and Anil K. Bajaj

***Abstract*—A unique T-beam microresonator designed to operate on the principle of nonlinear modal interactions due to 1 : 2 internal resonance is introduced. Specifically, the T-structure is designed to have two flexural modes with natural frequencies in a 1 : 2 ratio, and the higher frequency mode autoparametrically excites the lower frequency mode through inertial quadratic nonlinearities. A Lagrangian formulation is used to model the electrostatically actuated T-beam resonator, and it includes inertial quadratic nonlinearities, cubic nonlinearities due to midplane stretching and curvature of the beam, electrostatic potential, and effects of thermal prestress. A nonlinear two-mode reduced-order model is derived using linear structural modes in desired internal resonance. The model is used to estimate static pull-in bias voltages and dynamic responses using asymptotic averaging. Nonlinear frequency responses are developed for the case of resonant actuation of a higher frequency mode. It is shown that the lower frequency flexural mode is excited for actuation levels above a certain threshold and generates response component at half the frequency of resonant actuation. The effects of damping, thermal prestress, and mass and geometric perturbations from nominal design are thoroughly discussed. Finally, experimental results for a macroscale T-beam structure are briefly described and qualitatively confirm the basic analytical predictions. The T-beam resonator shows a high sensitivity to mass perturbations and, thus, holds great potential as a radio frequency filter–mixer and mass sensor. [2008-0107]**

***Index Terms*—Bifurcation, microresonators, nonlinear oscillators, reduced-order systems, resonator filters.**

I. Introduction

MICROELECTROMECHANICAL systems (MEMS) utilizing resonantly actuated structures or microresonators have a wide range of applications, such as chemical and biological sensors [1]–[4], pressure sensors [5], accelerometers [6], [7], gyroscopes [8], and radio frequency filters [9]–[11]. Most microresonators are excited in linear resonance. However, the inherent actuation and structural nonlinearities in the presence of high quality factors play an important role in the response of microresonators. For example, Shuiqing and Raman [12] reported chaotic response of the atomic force microscopy (AFM) cantilever probes, resulting in the deterioration of the AFM images. Huang *et al.* [13] concluded that the piezoelectric actuation nonlinearity results in AFM image deformations and consequently inaccurate interpretations of the geometric features. Younis and Nayfeh [14] developed a nonlinear model of an electrostatically actuated microresonator and compared their results with those of published experiments. They also found that the dynamic response is very sensitive to nonlinearities, and inaccurate representation of the nonlinearities can result in an error in the prediction of the resonator response. De and Aluru [15] studied chaotic motions of electrostatically actuated microresonators by including actuation nonlinearities. Kozinsky *et al.* [16] demonstrated tuning of nonlinearities and frequency through electrostatic actuation in a nanomechanical resonator.

Microresonators based on parametric resonances have also been reported in the literature [17], [18]. The response of a parametrically excited resonator remains bounded due to the nonlinearities in the system, and specifically, cubic nonlinearities play an important role [19]. The higher quality factor of microresonators, as compared to macrostructures, also enables the excitation in higher order parametric resonances [18]; however, microresonators operating in principal parametric resonance with excitation at twice the natural frequency are the most common. The response of a parametrically actuated structure shows a characteristic nonlinear phenomenon of sudden jump in amplitude as the excitation frequency is varied quasistatically. Zhang and Turner [20] utilized this nonlinear response for improving the sensitivity of a microresonator as a mass sensor. Rhoads *et al.* [21] designed a bandpass filter utilizing the nonlinear response of a parametrically excited microresonator.

In this paper, we present a unique microresonator design that, for the first time, utilizes structural inertial quadratic nonlinearities and nonlinear modal interactions for its functioning. Specifically, an electrostatically actuated T-beam microresonator configuration with two flexural modes in 1 : 2 internal resonance (natural frequencies in a 1 : 2 ratio) is considered. Though these two flexural modes are linearly uncoupled, the carefully designed T-beam configuration ensures that the two modes are coupled through inertial quadratic nonlinearities at the lowest order. The combination of 1 : 2 internally resonant modes and inertial quadratic nonlinearities then, in principle [19], result in the autoparametric excitation of the internally resonant lower frequency flexural mode when the other higher frequency mode is directly excited in resonance. More specifically, it is shown that it is possible to design a nonlinear microresonator such that the output is at nearly half the excitation frequency.

The microresonator design in this paper is motivated and guided by the literature on autoparametrically excited systems

Manuscript received April 24, 2008; revised December 30, 2008. First published May 5, 2009; current version published June 3, 2009. Subject Editor N. R. Aluru.

A. Vyas is with the School of Mechanical Engineering, Purdue University, West Lafayette, IN 47907-2088 USA, and also with Cummins Inc., Columbus, IN 47202-3005 USA (e-mail: ashwinv@purdue.edu).

D. Peroulis is with the Birck Nanotechnology Center, School of Electrical and Computer Engineering, Purdue University, West Lafayette, IN 47907-2057 USA (e-mail: dperouli@purdue.edu).

A. K. Bajaj is with the School of Mechanical Engineering, Purdue University, West Lafayette, IN 47907-2088 USA (e-mail: bajaj@purdue.edu).

Color versions of one or more of the figures in this paper are available online at http://ieeexplore.ieee.org.

Digital Object Identifier 10.1109/JMEMS.2009.2017081

[19], [22]–[25]. The nonlinear interactions of $1:2$ internally resonant modes and subsequent transfer of energy from a higher frequency mode to a lower frequency mode have been observed and demonstrated for several macro systems, such as an L-beam structure in [24], a cantilever attached to an oscillatory system [25], and pitch and roll mode interactions in ship dynamics [26], among others. The common features of such internally resonant systems are listed as follows: 1) two modes with natural frequencies in a $1:2$ ratio, e.g., $f/2$ and f; 2) quadratic nonlinearites, geometric or inertial, coupling the two modes; and 3) resonant excitation of mode at a higher frequency f. The resulting nonlinear interaction between the modes can result in transference of much of the input or excitation energy from the higher frequency mode to the lower frequency mode. The attenuation of the higher mode response is accompanied by a large amplitude response of the lower mode. This lower mode response is known to arise due to the parametric instability of the directly excited higher mode through a pitchfork bifurcation, and the lower mode response exists only in the frequency interval or band where the amplitude of actuated modes exceeds a certain threshold amplitude. Thus, the response of a microresonator working on this principle, specifically the output at half the excitation frequency, can be highly frequency selective and greater than the response amplitude of the directly excited mode. Potential applications of such a microresonator with these characteristics include biological and chemical sensors and RF filters.

A detailed nonlinear structural model of the T-beam resonator is developed using a Lagrangian formulation. The model also accounts for thermal residual stress or temperature changes in the beams. The nonlinearities in the model include inertial quadratic nonlinearities and structural cubic nonlinearities arising due to midplane stretching and beam curvature. Electrostatic actuation nonlinearities are retained to be able to estimate static pull-in voltages [27], [28] for the resonator. The analysis is based on a two-mode reduced-order model that is developed using analytical mode shapes obtained by a linearized model. The nonlinear dynamic response of the T-beam resonator about a statically deflected position, when responding to a harmonically oscillating voltage, is studied by an asymptotic method based on the method of averaging. The performance of a typical T-beam microresonator is illustrated by presenting analytical and simulation results. The effects of damping, thermal prestresses, higher order nonlinearities, addition of a small (compared to a T-beam structure) mass, and dimensional perturbations from nominal geometry needed for exact $1:2$ internal resonance are considered. Finally, the phenomenon of $1:2$ mode interaction and the basic predictions of the analytical model are verified qualitatively through an experiment with a macroscale T-structure.

This paper is organized as follows. A brief description of the system is given in Section II. Section III presents a nondimensional Lagrangian for the system that includes thermal prestresses and structural nonlinearities due to midplane stretching and beam curvature. Axial displacements of the beams are obtained using inextensibility and slender beam assumptions in Section IV. Section V presents linear analysis for the T-beam structure to determine design conditions for $1:2$ internal resonance of the first two modes. In Section VI, a two-mode approximate nonlinear model of the T-beam structure is developed, and slow-amplitude evolution equations governing the asymptotic response are derived. Section VII presents representative results on the response of the T-beam resonator along with the effects of model parameters. Section VIII presents essential results of experiments with a macroscale T-structure. Finally, Section IX gives some concluding remarks.

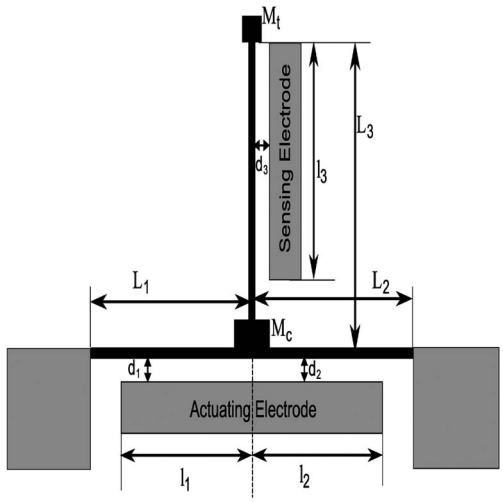

Fig. 1. T-shaped microresonator with rigid masses. The stationary parts of the structure are shown in gray. The actuating and sensing roles of the electrodes are switched, depending on the mode to be directly excited.

II. Description of the T-Beam Nonlinear Resonator

A schematic top view of the T-beam microresonator is shown in Fig. 1. The structure consists of three beams, with each of the "bottom" two beams anchored to the substrate at one of the ends. The lateral electrodes for actuation and sensing are also shown in the schematic. The bottom left beam is referred to as beam 1, the bottom right beam is referred to as beam 2, and the upper beam is referred to as beam 3. L_i and t_i denote, respectively, the length and thickness of the ith beam. M_c is a rigid mass at the joint of the three beams, and M_t is a rigid mass at the free end (tip) of the "upper" beam. To simplify the analysis, the rotary inertia of the rigid masses are taken into account without including the finiteness of these rigid masses. Furthermore, we neglect the rotary inertia of beams as we consider the operation of the structure such that only the lowest two modes, which are excited directly or indirectly, are involved.

A single electrode, referred to as electrode 1, is assumed to span over both the bottom beams. Electrode 1 is located at a distance d_1 and d_2 from bottom beams 1 and 2, respectively (see Fig. 1). We assume that the gaps d_1 and d_2 are equal. The lengths l_1 and l_2 denote the span of the electrode 1 over the bottom beams 1 and 2, respectively. Another stationary electrode, which is referred to as electrode 2, is assumed to be at a distance d_3 from the "upper" beam. The span of this electrode is l_3. In this model, V_{bj} represents the bias voltage on the jth electrode. Electrode 1 with ac voltage V_1 acts as an actuating electrode. Electrode 2 acts as a sensing electrode.

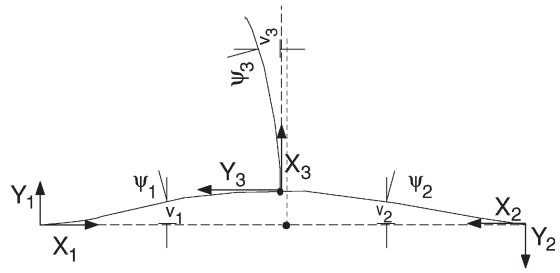

Fig. 2. Coordinate systems and beam displacements for the T-beam microresonator. (X_1, Y_1) is the reference coordinate system located at the left anchor, (X_2, Y_2) is the reference coordinate system located at the right anchor, and (X_3, Y_3) is the reference coordinate system for the vertical beam that is located at the displaced junction of the three beams.

The motion is assumed to be in the plane of the T-beam. The coordinate systems and displacements for the beam segments are shown in Fig. 2. Axial and transverse displacements of the ith beam element are denoted by u_i and v_i, respectively. The beam displacements are functions of undeformed arc length denoted by s_i. The displacements for the "bottom" beams are with respect to the anchored ends, and the displacements of the "upper" beam are measured with respect to the coordinate system located at the junction of the three beam segments. $\psi_i(s_i, t)$ denotes the rotation of the ith beam element. The shear deformation and warping are also assumed to be negligible as we are interested only in the low structural modes [29]. Thus, the rotations of the beam elements are given by

$$\sin\,\psi_i = \frac{\partial v_i}{\partial s_i}, \qquad i = 1, 2, 3. \tag{1}$$

Note that due to the nature of the boundary conditions, the upper beam can be assumed to be inextensible, whereas the bottom beams' models need to include midplane stretching nonlinearities. A Lagrangian description will now be used to model the T-beam resonator.

III. Nondimensional Lagrangian Formulation

A. Lagrangian Formulation

The kinetic energy T and potential energy P (including the electrostatic potential) of the system are given by

$$\left.\begin{aligned} T = &\left(\sum_{i=1}^{2}\int_0^{L_i}\tfrac{1}{2}m_i\left(\dot{u}_i^2+\dot{v}_i^2\right)ds_i\right)+\int_0^{L_3}\tfrac{1}{2}m_3\dot{\mathbf{r}}_{\mathbf{p}}.\dot{\mathbf{r}}_{\mathbf{p}}ds_3\\ &+\tfrac{1}{2}J_c\dot{\psi}_1^2\Big|_{s_1=L_1}+\tfrac{1}{2}J_t\dot{\psi}_3^2\Big|_{s_3=L_3}\\ &+\tfrac{1}{2}M_c\left(\dot{u}_1^2\Big|_{s_1=L_1}+\dot{v}_1^2\Big|_{s_1=L_1}\right)+\tfrac{1}{2}M_t(\dot{\mathbf{r}}_{\mathbf{p}}.\dot{\mathbf{r}}_{\mathbf{p}})\Big|_{s_3=L_3}\end{aligned}\right\} \tag{2}$$

$$\left.\begin{aligned} P = &\sum_{i=1}^{3}\int_0^{L_i}\tfrac{1}{2}(EI)_i\left(\tfrac{\partial\psi_i}{\partial s_i}\right)^2ds_i+\sum_{i=1}^{2}\int_0^{L_i}\tfrac{1}{2}(EA)_ie_{i0}^2ds_i\\ &-\tfrac{\epsilon_0\epsilon_r}{2}V_{b2}^2\left(\int_{L_3-l_3}^{L_3}\tfrac{1}{2}\tfrac{b_3}{d_3+v_3}ds_3\right)\\ &-\tfrac{\epsilon_0\epsilon_r}{2}\left(V_{b1}+V_1\cos(\Omega_1 t)\right)^2\\ &\times\left(\int_{L_1-l_1}^{L_1}\tfrac{b_1}{d_1+v_1}ds_1+\int_{L_2-l_2}^{L_2}\tfrac{b_2}{d_2-v_2}ds_2\right)\end{aligned}\right\} \tag{3}$$

where a dot denotes derivative with respect to time t, and a prime denotes derivative with respect to the corresponding beam arc length. $\dot{\mathbf{r}}_{\mathbf{p}}$ is the velocity of a point on beam 3 (the "upper" beam), and the dot product of the velocity, i.e., $\dot{\mathbf{r}}_{\mathbf{p}}.\dot{\mathbf{r}}_{\mathbf{p}}$, is given as follows:

$$\dot{\mathbf{r}}_{\mathbf{p}}.\dot{\mathbf{r}}_{\mathbf{p}} = \left(\dot{u}_1|_{s_1=L_1}-\dot{v}_3\right)^2+\left(\dot{v}_1|_{s_1=L_1}+\dot{u}_3\right)^2. \tag{4}$$

Furthermore, m_i and $(EI)_i$ are the mass per unit length and flexural rigidity of the ith beam in the lateral deflection, respectively. From here onward, we assume for simplicity that the beams are uniform. Furthermore, J_c and J_t are rotary inertias of the masses M_c and M_t, respectively, and b_i is the width (dimension in the direction toward substrate) of the ith beam. In (3), ϵ_0 and ϵ_r are the free-space permittivity $(8.8504\times10^{-12}$ F/m) and the dielectric constant of the material occupying the gaps ($\epsilon_r = 1$ for air gap), respectively.

Strain along the neutral axis of the ith beam is denoted by e_{i0}. Then, the effects of postfabrication residual stresses common in MEMS devices and temperature differences that may arise during usage are accounted for by including thermal strain for bottom beams as follows:

$$e_{j0} = \sqrt{\left(1+\frac{\partial u_j}{\partial s_j}\right)^2+\left(\frac{\partial v_j}{\partial s_j}\right)^2}-1-e_{Tj} \tag{5}$$

where $e_{Tj} = \alpha_{Tj}\Delta T_j$, $j = 1, 2$. Here, α_{Tj} is the coefficient of thermal expansion for the jth beam, and ΔT_j represents the temperature above the stress-free state.

The assumption that the upper beam is inextensible results in the following constraint on beam 3 displacements:

$$e_{30} = \sqrt{\left(1+\frac{\partial u_3}{\partial s_3}\right)^2+\left(\frac{\partial v_3}{\partial s_3}\right)^2}-1 = 0. \tag{6}$$

B. Nondimensionalization

We now introduce the following nondimensional parameters for the structural part of the resonator:

$$\left.\begin{aligned} &\hat{v}_i = \tfrac{v_i}{L} && \hat{u}_i = \tfrac{u_i}{L} && \bar{s}_i = \tfrac{s_i}{L_i}\\ &\alpha_i = \tfrac{(EI)_i}{EI} && r_i = \tfrac{m_i}{M} && \nu_i = \tfrac{L_i}{L}\\ &R_c = \tfrac{M_c}{(m_1L_1+m_2L_2)} && \gamma_c = \tfrac{J_c}{ML^3} && R_t = \tfrac{M_t}{m_3L_3}\\ &\gamma_t = \tfrac{J_t}{ML^3} && \kappa_i = t_i/L && \hat{b}_i = \tfrac{b_i}{L},\\ &i = 1,2,3 && \tau = \sqrt{\tfrac{EI}{ML^4}}t &&\\ &N_j = \tfrac{(EA)_j\kappa_j^2L^2}{EI}, && j = 1,2. &&\end{aligned}\right\} \tag{7}$$

Nondimensionalization is performed with respect to the following nominal parameters: 1) mass per unit length M; 2) length L; and 3) flexural rigidity EI. The arc length s_i of the ith beam is nondimensionalized with respect to the corresponding beam length; thus, $0 < \bar{s}_i < 1$. r_i is the ratio of mass per unit length of the ith beam to nominal mass per unit length. We also introduce variables t_i, $i = 1, 2, 3$, to denote the ith beam thickness in the Y_i direction (see Fig. 2). The parameters ν_i, κ_i, and $\hat{b}_i$, respectively, represent the ratios of the ith beam length,

thickness, and width to the nominal length. The nondimensional parameters (R_t, γ_t) and (R_c, γ_c) correspond to the rigid masses M_c and M_t, respectively. The parameter α_i denotes the ratio of flexural rigidity of the ith beam to the nominal flexural rigidity. The nondimensional axial rigidities are denoted by N_1 and N_2 for beams 1 and 2, respectively. τ denotes nondimensional time.

The nondimensional parameters related to electrostatic potential energy terms in (3) are defined as follows:

$$\left.\begin{aligned} g_i &= \frac{d_i}{L} \qquad \bar{l}_i = \frac{l_i}{L_i}, \\ i &= 1,2,3 \qquad \bar{\Omega}_1 = \Omega_1\sqrt{\frac{EI}{ML^4}} \\ &[F_{0j},\ F_{1j},\ F_{2j}]^T \\ &= \frac{L}{EI}\frac{\epsilon_0\epsilon_r b_1 L_1}{2d_1}\left[\left(V_{bj}^2+\frac{V_j^2}{2}\right),(2V_{bj}V_j),\left(\frac{V_j^2}{2}\right)\right]^T, \\ &\qquad j=1,2 \end{aligned}\right\} \tag{8}$$

with $V_2 = 0$. Here, g_i is the nondimensional gap between the ith beam and the corresponding adjacent stationary electrode; $\bar{l}_i$ is the nondimensional span of the electrode over the ith beam; F_{0j} corresponds to the static force due to the jth electrode, and F_{11} and F_{21} correspond to the harmonic force components, with nondimensional frequencies $\bar{\Omega}_1$ and $2\bar{\Omega}_1$, respectively, which are generated due to the voltage applied to electrode 1.

Then, using the nondimensional parameters [see (7) and (8)], expressions for nondimensional kinetic and potential energies can be obtained.

Along with the kinetic and potential energies of the system, constraints on the beam segment slopes and displacements at their junctions have to be satisfied. To account for all these constraints in a compact formulation, we can define an augmented Lagrangian, which is denoted by L_{aug}, as follows:

$$\left.\begin{aligned} L_{\text{aug}} = \hat{T}-\hat{P}+\frac{1}{2}\int_0^{L_3}\lambda_1 \\ \times\left(\left(1+\frac{1}{\nu_3}\frac{\partial\hat{u}_3}{\partial\bar{s}_3}\right)^2+\left(\frac{1}{\nu_3}\frac{\partial\hat{v}_3}{\partial\bar{s}_3}\right)^2-1\right)ds_3 \\ +\lambda_2(\hat{u}_1|_{\bar{s}_1=1}+\hat{u}_2|_{\bar{s}_2=1})+\lambda_3(\hat{v}_1|_{\bar{s}_1=1}+\hat{v}_2|_{\bar{s}_2=1}) \\ +\lambda_4(\hat{\psi}_1|_{\bar{s}_1=1}-\hat{\psi}_2|_{\bar{s}_2=1})+\lambda_5(\hat{\psi}_1|_{\bar{s}_1=1}-\hat{\psi}_3|_{\bar{s}_3=0}) \end{aligned}\right\} \tag{9}$$

where the Lagrange multiplier λ_1 imposes the inextensibility constraint for beam 3, and the Lagrange multipliers $\lambda_2, \ldots, \lambda_5$ ensure that the three beam segments have the same displacements and slopes at their junctions. This augmented Lagrangian will be utilized later to obtain the exact description of the linearized model to define the required mode shapes and natural frequencies of the T-resonator.

IV. Axial Displacements

In the formulation so far, the displacements $\hat{u}_3$ and $\hat{v}_3$ are not independent if the inextensibility constraint is utilized. Thus, the model equations can be simplified further, as usual in nonlinear structural dynamics [29]. We follow these arguments and developments carefully for each of the three component beams. Axial displacement of beam 3, i.e., the "upper" beam, is related to its transverse displacement by the inextensibility constraint $\hat{e}_{30} = 0$ in (6). Integrating the inextensibility constraint and imposing the boundary condition $\hat{u}_3 = 0$ at the junction, $\bar{s}_3 = 0$, gives

$$\hat{u}_3 = -\frac{1}{2}\int_0^{\bar{s}_3}\frac{\hat{v}_3'^{\,2}}{\nu_3}d\bar{s}_3 \tag{10}$$

where a prime denotes derivative with respect to the corresponding arc length.

To find axial displacements of beams 1 and 2, first, the equations of motion governing axial displacements are obtained using Hamilton's principle [30]. Assuming the beams to be slender, we assume that the inertial terms due to axial displacements $\hat{u}_1$ and $\hat{u}_2$ are negligible, and that the curvature nonlinearities are negligible in comparison to the stretching nonlinearities. Using these assumptions, the following equation is obtained for axial displacements $\hat{u}_1$ and $\hat{u}_2$:

$$\left(\hat{u}_i'+\frac{1}{2}\frac{\hat{v}_3'^{\,2}}{\nu_i}-\nu_i e_{Ti}\right)' = 0, \qquad i=1,2 \tag{11}$$

along with the following boundary conditions:

$$\left.\begin{aligned} &\hat{u}_1|_{\bar{s}_1=0}=0 \quad \hat{u}_2|_{\bar{s}_2=0}=0 \quad \hat{u}_1|_{\bar{s}_1=1}+\hat{u}_2|_{\bar{s}_2=1}=0 \\ &\sum_{i=1}^{2}(-1)^i\frac{N_i}{\kappa_i^2\nu_i}\left(\hat{u}_i'+\frac{1}{2}\frac{\hat{v}_3'^{\,2}}{\nu_i}-\nu_i e_{Ti}\right)=0. \end{aligned}\right\} \tag{12}$$

The last boundary condition in (12) arises from the balance of axial forces at the junction of the three beams. The other three boundary conditions are for the clamped ends of the beams at $\bar{s}_1 = 0$ and $\bar{s}_2 = 0$ and the continuity of the axial displacement at the junction.

Integrating (11) and imposing the boundary conditions in (12) result in the following expression for axial displacements:

$$\hat{u}_i = -\frac{1}{2}\int_0^{\bar{s}_i}\frac{\hat{v}_3'^{\,2}}{\nu_i}d\bar{s}_i + C_i(\tau)\bar{s}_i + \nu_i e_{Ti}\bar{s}_i, \qquad i=1,2 \tag{13}$$

where C_1 and C_2 are functions of time τ, which is given as follows:

$$\left.\begin{aligned} C_i(\tau) &= J_i\sum_{j=1}^{2}\left(\left(\frac{1}{2}\int_0^1\frac{\hat{v}_3'^{\,2}}{\nu_j}d\bar{s}_j\right)-\nu_j e_{Tj}\right), \qquad i=1,2 \\ [J_1,J_2]^T &= \frac{1}{\nu_1 N_2\kappa_1^2+\nu_2 N_1\kappa_2^2}\left[\nu_1 N_2\kappa_1^2, \nu_2 N_1\kappa_2^2\right]^T \end{aligned}\right\} \tag{14}$$

where J_1 and J_2 are introduced to keep the expressions compact.

The axial displacements thus derived can now be substituted in the system kinetic and potential energies, thereby eliminating the axial displacements from ultimate consideration of nonlinear dynamics of the structure. Note that the inertial and

curvature nonlinearities arising from the "bottom" beams' deflections are neglected. The resulting system Lagrangian, i.e., $\hat{L}$, in nondimensional variables and with up to quartic terms retained in the mechanical energy part is given as follows:

$$\begin{aligned}\hat{L}=&\frac{1}{2}\left(\sum_{i=1}^{3}\int_0^1 r_i\nu_i\dot{\hat{v}}_i^2 d\bar{s}_i\right)\\&+\frac{1}{2}\left(\frac{\gamma_c}{\nu_1^2}\dot{\hat{v}}_1'^2|_{\bar{s}_1=1}+\frac{\gamma_t}{\nu_3^2}\dot{\hat{v}}_3'^2|_{\bar{s}_3=1}+R_t r_3\nu_3\dot{\hat{v}}_3^2|_{\bar{s}_3=1}\right)\\&+\frac{1}{2}\left(R_c(r_1\nu_1+r_2\nu_2)+R_t r_3\nu_3+\int_0^1 r_3\nu_3 d\bar{s}_3\right)\\&\times\dot{\hat{v}}_1^2|_{\bar{s}_1=1}+R_t r_3\nu_3\left(\dot{\hat{v}}_1|_{\bar{s}_1=1}\dot{\hat{u}}_3-\dot{\hat{u}}_1|_{\bar{s}_1=1}\dot{\hat{v}}_3\right)|_{\bar{s}_3=1}\\&+\int_0^1 r_3\nu_3(\dot{\hat{v}}_1|_{\bar{s}_1=1}\dot{\hat{u}}_3-\dot{\hat{u}}_1|_{\bar{s}_1=1}\dot{\hat{v}}_3)d\bar{s}_3\\&+\frac{1}{2}\Bigg(R_t r_3\nu_3\dot{\hat{u}}_3^2\\&\qquad-2\frac{\gamma_t}{\nu_3^3}\left(\dot{\hat{u}}_3'\dot{\hat{v}}_3'\hat{v}_3'+\hat{u}_3'\dot{\hat{v}}_3'^2+\hat{v}_3'^2\hat{v}_1'^2\right)\Bigg)|_{\bar{s}_3=1}\\&+\frac{1}{2}\int_0^1 r_3\nu_3\dot{\hat{u}}_3^2 d\bar{s}_3\\&-\frac{1}{2}\left(\left(\sum_{i=1}^{3}\int_0^1\frac{\alpha_i}{\nu_i^3}\hat{v}_3''^2 d\bar{s}_i\right)+\int_0^1\frac{\alpha_3}{\nu_3^4}\hat{v}_3'^2\hat{v}_3''^2 d\bar{s}_3\right)\\&-\frac{1}{2}\left(\sum_{i=1}^{2}\int_0^1\frac{N_i}{\kappa_i^2\nu_i}\left(\hat{u}_i'+\frac{1}{2}\frac{\hat{v}_3'^2}{\nu_i}-\nu_i e_{Ti}\right)^2 d\bar{s}_i\right)\\&+(F_{01}+F_{11}\cos\bar{\Omega}_1\tau+F_{21}\cos 2\bar{\Omega}_1\tau)\\&\times\left(\int_{1-\bar{l}_1}^1\frac{\nu_1}{1+(\hat{v}_1/g_1)}d\bar{s}_1+\int_{1-\bar{l}_2}^1\frac{\hat{b}_2}{\hat{b}_1}\frac{g_1}{g_2}\frac{\nu_2}{1-(\hat{v}_2/g_2)}d\bar{s}_2\right)\\&+F_{02}\left(\int_{1-\bar{l}_3}^1\frac{\hat{b}_3}{\hat{b}_1}\frac{g_1}{g_3}\frac{\nu_3}{1+(\hat{v}_3/g_3)}d\bar{s}_3\right)\end{aligned}\tag{15}$$

where a dot now represents derivative with respect to time τ.

V. Linear Analysis

We first perform a linear analysis to obtain the mode shapes and natural frequencies of the system with no electrostatic actuation. The appropriately reduced Lagrangian in (15), with up to quadratic terms and with the use of Hamilton's principle [30], gives the following three linear equations of motion for transverse displacements:

$$\ddot{\hat{v}}_i+\frac{N_i}{r_i\nu_i^3\kappa_i^2}J_i(\nu_1 e_{T1}+\nu_2 e_{T2})\frac{\partial^2\hat{v}_i}{\partial\bar{s}_i^2}+\frac{\alpha_i}{r_i\nu_i^4}\frac{\partial^4\hat{v}_i}{\partial\bar{s}_i^4}=0\quad i=1,2$$

$$\ddot{\hat{v}}_3+\frac{\alpha_3}{r_3\nu_3^4}\frac{\partial^4\hat{v}_3}{\partial\bar{s}_3^4}=0.\tag{16}$$

As for the boundary conditions, the slope and displacement of the bottom beams 1 and 2 are zero at $\bar{s}_1=0$ and $\bar{s}_2=0$. Furthermore, the displacement of the upper beam, i.e., $\hat{v}_3=0$, is zero at $\bar{s}_3=0$. The remaining boundary conditions are

$$\left.\frac{\partial\hat{v}_1}{\partial\bar{s}_1}\right|_{\bar{s}_1=1}=\left.\frac{\nu_1}{\nu_2}\frac{\partial\hat{v}_2}{\partial\bar{s}_2}\right|_{\bar{s}_2=1}\tag{17}$$

$$\hat{v}_1|_{\bar{s}_1=1}=-\hat{v}_2|_{\bar{s}_2=1}\tag{18}$$

$$\left.\frac{\partial\hat{v}_1}{\partial\bar{s}_1}\right|_{\bar{s}_1=1}=\left.\frac{\nu_1}{\nu_3}\frac{\partial\hat{v}_3}{\partial\bar{s}_3}\right|_{\bar{s}_3=0}\tag{19}$$

$$\begin{aligned}&(\nu_1 e_{T1}+\nu_2 e_{T2})\left(\tfrac{N_1}{\kappa_1^2\nu_1^2}J_1\left.\tfrac{\partial\hat{v}_1}{\partial\bar{s}_1}\right|_{\bar{s}_1=1}-\tfrac{N_2}{\kappa_2^2\nu_2^2}J_2\left.\tfrac{\partial\hat{v}_2}{\partial\bar{s}_2}\right|_{\bar{s}_2=1}\right)\\&\quad+\left.\tfrac{\alpha_1}{\nu_1^3}\tfrac{\partial^3\hat{v}_1}{\partial\bar{s}_1^3}\right|_{\bar{s}_1=1}-\left.\tfrac{\alpha_2}{\nu_2^3}\tfrac{\partial^3\hat{v}_2}{\partial\bar{s}_2^3}\right|_{\bar{s}_2=1}\\&\quad=((1+R_t)r_3\nu_3+R_c(r_1\nu_1+r_2\nu_2))\left.\ddot{\hat{v}}_1\right|_{s_1=1}\end{aligned}\tag{20}$$

$$\left.\frac{\alpha_3}{\nu_3^2}\frac{\partial^2\hat{v}_3}{\partial\bar{s}_3^2}\right|_{\bar{s}_3=0}-\left.\frac{\alpha_1}{\nu_1^2}\frac{\partial^2\hat{v}_1}{\partial\bar{s}_1^2}\right|_{\bar{s}_1=1}-\left.\frac{\alpha_2}{\nu_2^2}\partial^2\frac{\hat{v}_2}{\partial\bar{s}_2^2}\right|_{\bar{s}_2=1}=\left.\frac{\gamma_c}{\nu_1}\frac{\partial^3\hat{v}_1}{\partial\tau^2\partial\bar{s}_1}\right|_{\bar{s}_1=1}\tag{21}$$

$$\left.\frac{\alpha_3}{\nu_3^3}\frac{\partial^3\hat{v}_3}{\partial\bar{s}_3^3}\right|_{\bar{s}_3=1}=\left.R_t r_3\nu_3\ddot{\hat{v}}_3\right|_{s_3=1}\tag{22}$$

$$\left.\frac{\alpha_3}{\nu_3}\frac{\partial^2\hat{v}_3}{\partial\bar{s}_3^2}\right|_{\bar{s}_3=1}=-\gamma_t\left.\frac{\partial^3\hat{v}_3}{\partial\tau^2\partial\bar{s}_3}\right|_{s_3=1}.\tag{23}$$

A. Analytical Mode Shapes and Natural Frequencies

The linear mode shapes and natural frequencies can be obtained by separation of variables as follows:

$$\hat{v}_i(\bar{s}_i,t)=\Upsilon_i(\bar{s}_i)\exp(\sqrt{-1}\omega\tau),\qquad i=1,2,3\tag{24}$$

where Υ_i is a spatial function, and ω is the natural frequency associated with the mode shape Υ_i. In addition, from here onward, we make the following assumptions: 1) the temperature changes and the coefficient of thermal expansions for beams 1 and 2 are the same, and thus, $e_{T1}=e_{T2}=e_T$; 2) the axial rigidities of beams 1 and 2 are the same, and thus, $N_1=N_2=N$; and 3) the thicknesses of beams 1 and 2 are the same, and thus, $\kappa_1=\kappa_2=\kappa$. To keep the equations concise, we introduce a parameter S_T that represents the nondimensional thermal stress in the bottom beams, which is defined as

$$S_T=\frac{N}{\kappa^2}e_T.\tag{25}$$

Separating space and time parts, we find that the following solution satisfies the governing equations:

$$\begin{aligned}\Upsilon_i(\bar{s}_i)=&\varphi_{1i}\cos\beta_{i1}\bar{s}_i+\varphi_{2i}\sin\beta_{i1}\bar{s}_i\\&+\varphi_{3i}\cosh\beta_{i2}\bar{s}_i+\varphi_{4i}\sinh\beta_{i2}\bar{s}_i\end{aligned}\tag{26}$$

where $i = 1, 2, 3$, and $\beta_{i(1/2)}$ are given by

$$\beta^2_{j(1/2)} = \frac{r_j \nu_j^4}{2\alpha_j}\left(\pm\frac{S_T}{r_j\nu_j^2} + \sqrt{\left(\frac{S_T}{r_j\nu_j^2}\right)^2 + \frac{4\alpha_j\omega^2}{r_j\nu_j^4}}\right), \qquad j = 1, 2$$

$$\beta^4_{31} = \beta^4_{32} = \frac{r_3\nu_3^4\omega^2}{\alpha_3}. \tag{27}$$

The boundary conditions are used now to determine a characteristic matrix and, thereby, natural frequencies, ω, and coefficients φ_{ij}. Thus, linear mode shapes and natural frequencies are obtained analytically.

B. Illustrative Results of Linear Analysis

Consider a specific system with no rigid masses and all three beams having the same mass per unit length and flexural rigidity. We assume that there is no residual stress in beams 1 and 2, i.e., $N_1 = N_2 = 0$. Furthermore, we assume that the lengths of the "bottom" beams are equal, i.e., $L_1 = L_2$ or $\nu_1 = \nu_2$. The natural frequencies of the system are now computed analytically as a function of the length fraction (ν_3/ν_1). It is found that when the ratio of the length of the upper beam to the length of one of the bottom beams is 1.3266, the first and second natural frequencies of the structure are in a $1:2$ ratio. This provides us with an important design condition for the nonlinear system to possibly have $1:2$ internal resonance.

An ANSYS finite-element method (FEM) model of the T-beam structure with no electrostatic actuation is used to verify the above nondimensional linear analysis. Beam elements are used in modeling the structure in ANSYS. The dimensions of the structure with material properties of polysilicon are chosen to be

$$\left.\begin{array}{ll} L_1 = 100\ \mu\text{m} & L_3 = 100\frac{\nu_3}{\nu_1}\ \mu\text{m} \\ t_1 = 3\ \mu\text{m} & b_1 = 5\ \mu\text{m} \\ E_1 = 169\times 10^9\ \text{N/m}^2 & \rho = 2330\ \text{kg/(m}^3) \end{array}\right\}. \tag{28}$$

Furthermore, all the beams have the same cross-sectional area and are made of the same material. The first four natural frequencies for this system as a function of the length ratio ν_3/ν_1 are shown in Fig. 3. The analytically computed lowest two modes for the critical length ratio $(\nu_3/\nu_1) = 1.3266$ are shown in Fig. 4. In the first mode, the bottom beams undergo only a small transverse vibration as compared to the upper beam. However, in the second mode, only the two lower beams undergo transverse deflection, and the transverse displacement of the upper beam is zero. In this second mode, the upper beam only has axial or rigid body motion in absolute coordinates. Due to the nature of these T-beam modes, note that the only way that the upper beam will undergo transverse deflection is when the response of the structure has some contribution from the first mode. If the structure is excited near the second mode frequency, this can happen only when energy is transferred from the second mode to the first mode through $1:2$ internal resonance. This linear spatial decoupling between the two modes is a very important characteristic of the T-shaped microresonator as the second mode actuation using electrode 1 will result in no capacitive current at electrode 2, unless the energy gets transferred from the second mode to the first mode due to nonlinear modal interactions through internal resonance.

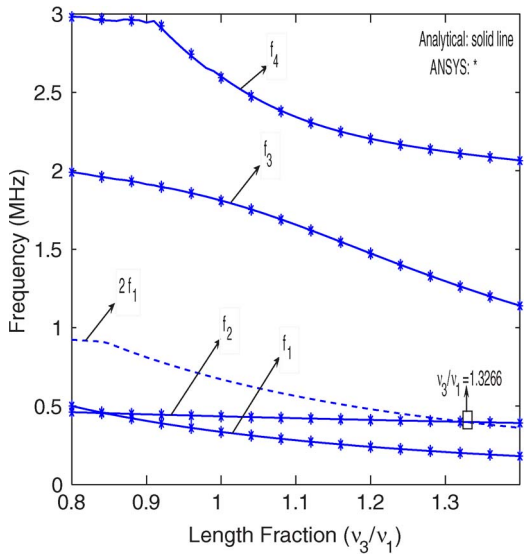

Fig. 3. First four natural frequencies, represented by $f_i = (\omega_i/2\pi)$, of the T-beam structure as a function of the length ratio (L_3/L_1) or (ν_3/ν_1). T-beam structure parameters are given as follows: no rigid masses $(R_c = \gamma_c = R_t = \gamma_t = 0)$; equal mass per unit lengths $(r_1 = r_2 = r_3)$; equal flexural rigidities $(\alpha_1 = \alpha_2 = \alpha_3)$; and equal lengths of the bottom beams $(\nu_1 = \nu_2)$. (Solid line) Analytically computed frequencies. $(*)$ Frequencies computed using the ANSYS FEM model of the structure. $\omega_2 = 2\omega_1$ at $(\nu_3/\nu_1) = 1.3266$.

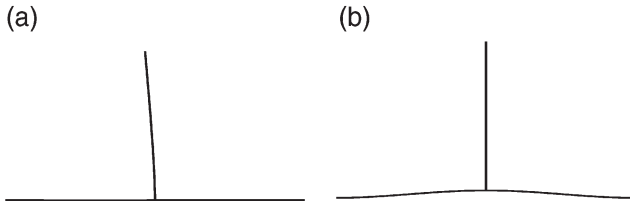

Fig. 4. First two modes of the T-beam structure when the length ratio (L_3/L_1) or (ν_3/ν_1) is equal to 1.3266. Other parameters for this T-beam structure are given as follows: no rigid masses $(R_c = \gamma_c = R_t = \gamma_t = 0)$; equal mass per unit lengths $(r_1 = r_2 = r_3)$; equal flexural rigidities $(\alpha_1 = \alpha_2 = \alpha_3)$; and equal lengths of the bottom beams $(\nu_1 = \nu_2)$. (a) First mode. (b) Second mode.

VI. Nonlinear Response Under Resonant Excitation

To study the nonlinear response of the T-beam structure, modal expansion is now used to develop a reduced-order model of the resonator, and the analytical mode shapes determined above are used in this expansion. Since the modes not excited directly by external resonance or indirectly through internal resonance are expected to decay due to the presence of damping [19], [26], the long-term behavior (including steady-state response) can be studied by retaining the two directly and indirectly excited modes in modal expansion. Thus, for the ith beam displacement, we can write

$$\hat{v}_i = \epsilon(A_1\phi_{1i} + A_2\phi_{2i}), \qquad i = 1, 2, 3 \tag{29}$$

where A_i are functions of time, and ϕ_{1i} and ϕ_{2i} are the ith beam spatial functions in the first and second modes, respectively. Substituting this modal expansion for beam displacements in the system Lagrangian in (15) and spatially averaging it over the domain, the following averaged Lagrangian [19], [24] is obtained:

$$\begin{aligned}\hat{L} =& \Gamma_{11}\dot{A}_1^2 + \Gamma_{22}\dot{A}_2^2 + 2\Gamma_{12}\dot{A}_1\dot{A}_2 \\ &+ \left(\sum_{i=0}^{1}\sum_{j=0}^{2} Q_{ij}A_1^{1-i}A_2^i\dot{A}_1^{2-j}\dot{A}_2^j\right) \\ &+ \left(\sum_{i=0}^{2}\sum_{j=0}^{2} \Theta_{ij}A_1^{2-i}A_2^i\dot{A}_1^{2-j}\dot{A}_2^j\right) \\ &- W_{11}A_1^2 - W_{22}A_2^2 - 2W_{12}A_1A_2 - \left(\sum_{i=0}^{4} K_iA_1^{4-i}A_2^i\right) \\ &+ (F_{01} + F_{11}\cos\bar{\Omega}_1\tau + F_{21}\cos 2\bar{\Omega}_1\tau) \\ &\times \left(\sum_{i=0}^{n+1}\sum_{j=1}^{i+1} f_{ij}A_1^{i+1-j}A_2^{i-1}\right) \\ &+ F_{02}\left(\sum_{i=0}^{n+1}\sum_{j=1}^{i+1} h_{ij}A_1^{i+1-j}A_2^{i-1}\right). \end{aligned} \tag{30}$$

Note that the above averaged Lagrangian is only time dependent and depends on two degrees of freedom defined by the modal amplitudes of the two interacting given modes. The parameters Γ_{11}, Γ_{22}, Γ_{12}, W_{11}, W_{22}, and W_{12} are the coefficients of quadratic terms due to the structural part of energy, Q_{ij}s (with $i = 0, 1$ and $j = 0, 1, 2$) are the coefficients of inertial cubic nonlinearities, Θ_{ij}s (with $i = 0, 1, 2$ and $j = 0, 1, 2$) are the coefficients of inertial quartic nonlinearities, and K_is (with $i = 0, 1, 2, 3, 4$) are the coefficients of stretching and curvature quartic nonlinearities. Actuation nonlinearities up to an arbitrary order n are retained in the Lagrangian. Higher order terms in electrostatic potential are relevant mainly for estimating the static equilibrium position of the structure under applied bias voltages and for estimating the static pull-in voltage. The expressions for Γ_{ij}, W_{ij}, Q_{ij}, Θ_{ij}, K_i, f_{ij}, and h_{ij} in terms of the modal functions are given in the Appendix. Also note that the mode shapes for a nominal design are scaled such that $\Gamma_{11} = \Gamma_{22} = 1/2$. Finally, recall that F_{01} and F_{02} represent electrostatic bias voltages, and F_{ij}, $i = 1, 2$, represent the harmonic components of excitation.

A. Static Equilibrium Equations

Electrostatic forces due to bias voltages result in deflecting the beams from the zero (or undeformed) equilibrium position. The equations governing static equilibrium deflection of a T-resonator structure obtained using the Lagrangian are given as follows:

$$\begin{aligned} &2W_{11}A_{10} + 2W_{12}A_{20} + \sum_{i=0}^{3}(4-i)K_iA_{10}^{3-i}A_{20}^i \\ &\quad = \sum_{i=1}^{n}\sum_{j=1}^{i}(i+1-j)A_{10}^{i-j}A_{20}^{i-1}(F_{01}f_{ij} + F_{02}h_{ij}) \\ &2W_{22}A_{20} + 2W_{12}A_{10} + \sum_{i=1}^{4} iK_iA_{10}^{4-i}A_{20}^{i-1} \\ &\quad = \sum_{i=1}^{n}\sum_{j=2}^{i+1}(i-1)A_{10}^{i+1-j}A_{20}^{i-2}(F_{01}f_{ij} + F_{02}h_{ij}) \end{aligned} \tag{31}$$

where A_{10} and A_{20} are the static equilibrium modal amplitudes. The equations in (31) comprise a set of two coupled nonlinear equations for the deflection amplitudes A_{10} and A_{20} and can be used to obtain static pull-in voltages [28], [31]. The static pull-in voltage results predicted for a typical T-resonator will be presented in the next section. These will be important to assure that the bias voltages utilized for the operation of the resonator remain sufficiently small compared to the pull-in voltages.

In the resonant mode of operation for the T-beam structure, we set the bias voltages much lower than the pull-in voltages. As a result, the static deflections can be approximated by assuming a power series solution in terms of the powers of bias voltages F_{01} and F_{02}, and thus, we get

$$A_{i0} = \mu_{i0} + \mu_{i1}F_{01} + \mu_{i2}F_{02} + \sum_{j=3}^{5}\mu_{ij}F_{01}^{5-j}F_{02}^{j-3} + \text{h.o.t.}, \quad i = 1, 2 \tag{32}$$

where h.o.t. stands for higher order terms, and μ_{ij} are the power series coefficients. Balancing the zeroth-order powers of F_{01} and F_{02} in equilibrium equations gives nonlinear equations for coefficients μ_{10} and μ_{20}, with $\mu_{10} = \mu_{20} = 0$ as one of the possible solutions. Assuming the beams to be without any initial curvature, it is natural to set $\mu_{10} = \mu_{20} = 0$. The coefficients μ_{11} and μ_{21} in the power series are obtained by balancing the first-order powers of F_{01} and F_{02}, and these are

$$\begin{aligned}[\mu_{11}, \mu_{21}]^T &= \frac{1}{4(W_{11}W_{22} - W_{12}^2)} \\ &\quad \times [2W_{22}f_{11} - 2W_{12}f_{12}, -2W_{12}f_{11} + 2W_{11}f_{12}]^T \\ [\mu_{12}, \mu_{22}]^T &= \frac{1}{4(W_{11}W_{22} - W_{12}^2)} \\ &\quad \times [2W_{22}h_{11} - W_{11}h_{12}, -2W_{12}h_{11} + 2W_{11}h_{12}]^T. \end{aligned} \tag{33}$$

Similarly, higher order terms in the expansions in (32) can be evaluated easily. For our nonlinear analysis near resonances with small bias voltages (much less than pull-in voltages), linear approximations of static deflections will be seen to be sufficient.

B. Scalings and Equations of Motion

In the resonator mode of operation, the total response comprises of the static deflection and an oscillatory motion about

the static equilibrium. Further, in the nonlinear analysis, we are interested in studying the response of the resonator for small but finite amplitude oscillations. As a result, we assume the following scaled form of modal amplitudes and actuation forces:

$$A_i = A_{i0} + \epsilon a_i(\tau) \quad F_{0i} = \epsilon \hat{F}_{0i} \quad F_{j1} = \epsilon^2 \hat{F}_{j1} \tag{34}$$

where $i = 1, 2$, $j = 1, 2$, and ϵ is a nondimensional scaling parameter with $0 < \epsilon \ll 1$. Here, a_1 and a_2 are the time-dependent oscillatory components of modal amplitudes A_1 and A_2, respectively. The scaling for actuation forces implies that the nonlinear analysis is for the case of weak excitation. The static actuation force parameters F_{0j} are scaled to make explicit the assumption that the bias voltages are much lower than the pull-in voltages, and thus, the static deflection amplitudes, denoted by A_{i0}, are also small. In addition, the scaling ϵ also serves as an ordering parameter in the equations of motion.

The resonator's dimensions and properties can be different from the designed (nominal) microresonator due to many reasons, e.g., fabrication uncertainties, addition of a mass particle, or an increase in temperature during or after fabrication. These small perturbations in beam lengths, residual stresses, and tip masses from the corresponding nominal parameters are now included in the resonator model through deviations from their nominal values. We have

$$\begin{aligned} \nu_3 &= \nu_{30}(1 + \epsilon\sigma_{L_3}) \quad \nu_2 = \nu_{20}(1 + \epsilon\sigma_{L_2}) \\ R_t &= R_{t0} + \epsilon\hat{R}_t \qquad S_T = S_{T0} + \epsilon\hat{S}_T. \end{aligned} \tag{35}$$

Here, σ_{L_3} and σ_{L_2} represent perturbations in beam 2 and 3 length fractions, respectively, from the corresponding nominal length fractions. The nominal parameters are indicated by the subscript "0" in the above representation. $\hat{R}_t$ denotes perturbation due to addition of a small mass at the tip of beam 3. $\hat{S}_T$ accounts for variation in the residual stress from the nominal residual stress.

C. Equations of Motion for the Two-Mode Model

Substituting the scaled modal amplitudes, actuation forces, and perturbed system parameters in the system Lagrangian in (30) and using the definitions of Lagrange's equations, the following equations of motion are obtained:

$$\begin{aligned} &\ddot{a}_i + \omega_i^2 a_i + \epsilon\Big(2\hat{\zeta}_i\omega_i\dot{a}_i + \eta_{i1}a_1 + \eta_{i2}a_2 + \eta_{i3}a_1^2 + \eta_{i4}a_2^2 \\ &\qquad + \eta_{i5}a_1a_2 + \eta_{i6}\dot{a}_1^2 + \eta_{i7}\dot{a}_2^2 + \eta_{i8}\dot{a}_1\dot{a}_2\Big) \\ &\quad = \epsilon\frac{1}{2\Gamma_{ii}|_{\epsilon=0}}\Big(f_{1i}(\hat{F}_{11}\cos(\bar{\Omega}_1\tau) + \hat{F}_{21}\cos(2\bar{\Omega}_1\tau)\Big) + O(\epsilon^2) \end{aligned} \tag{36}$$

where $i = 1, 2$. In these equations, terms of $O(\epsilon^2)$ and higher are not explicitly depicted as they will not contribute to the first-order asymptotic approximation of nonlinear response. In addition, the accelerations $\ddot{a}_i$s in the nonlinear terms on the right-hand side are approximated by $-\omega_i^2 a_i$s. Note further that in these equations, viscous damping has been introduced, with $\hat{\zeta}_i$ being the scaled modal damping coefficient for the ith mode. The scaled damping is related to the ith mode modal damping ζ_i by

$$\zeta_i = \epsilon\hat{\zeta}_i, \qquad i = 1, 2. \tag{37}$$

The scaling of damping coefficients implies that the system is assumed to be lightly damped. The natural frequencies ω_is for the two-mode model are

$$\omega_i^2 = \left.\frac{W_{ii}}{\Gamma_{ii}}\right|_{\epsilon=0}, \qquad i = 1, 2 \tag{38}$$

where the parameters W_{ii} and Γ_{ii} are already defined in averaged Lagrangian in (30). Note that the modal amplitude equations are uncoupled at the zeroth-order because exact mode shapes of the nominal structure have been used in modal expansion.

To first order (in ϵ), only the parameters η_{11} and η_{22} affect the natural frequencies, and these parameters are given by

$$\begin{aligned} \eta_{11} &= \left(\frac{1}{\Gamma_{11}}\Big(S_{11}\sigma_{L_3} + S_{12}\sigma_{L_2} + S_{13}\hat{R}_t \right. \\ &\qquad + S_{14}\hat{S}_T - \omega_1^2(Q_{00}\bar{A}_{10} + Q_{10}\bar{A}_{20}) \\ &\qquad \left. - (f_{21}\hat{F}_{01} + h_{21}\hat{F}_{02})\Big)\right)\Big|_{\epsilon=0} \\ \eta_{22} &= \left(\frac{1}{\Gamma_{22}}\Big(S_{21}\sigma_{L_3} + S_{22}\sigma_{L_2} + S_{23}\hat{R}_t \right. \\ &\qquad + S_{24}\hat{S}_T - \omega_2^2(Q_{02}\bar{A}_{10} + Q_{12}\bar{A}_{20}) \\ &\qquad \left. - (f_{23}\hat{F}_{01} + h_{23}\hat{F}_{02})\Big)\right)\Big|_{\epsilon=0} \end{aligned} \tag{39}$$

where

$$\begin{aligned} \bar{A}_{i0} &= \mu_{i1}\hat{F}_{01} + \mu_{i2}\hat{F}_{02} \\ S_{i1} &= \left(-\omega_i^2\frac{\partial^2\Gamma_{ii}}{\partial\sigma_{L_3}\partial\epsilon} + \frac{\partial^2 W_{ii}}{\partial\sigma_{L_3}\partial\epsilon}\right)\Big|_{\epsilon=0} \\ S_{i2} &= \left(-\omega_i^2\frac{\partial^2\Gamma_{ii}}{\partial\sigma_{L_2}\partial\epsilon} + \frac{\partial^2 W_{ii}}{\partial\sigma_{L_2}\partial\epsilon}\right)\Big|_{\epsilon=0} \\ S_{i3} &= \left(-\omega_i^2\frac{\partial^2\Gamma_{ii}}{\partial\hat{R}_t\partial\epsilon} + \frac{\partial^2 W_{ii}}{\partial\hat{R}_t\partial\epsilon}\right)\Big|_{\epsilon=0} \\ S_{i4} &= \left(-\omega_i^2\frac{\partial^2\Gamma_{ii}}{\partial\hat{S}_t\partial\epsilon} + \frac{\partial^2 W_{ii}}{\partial\hat{S}_t\partial\epsilon}\right)\Big|_{\epsilon=0}, \qquad i = 1, 2. \end{aligned} \tag{40}$$

The effect of variations in the system parameters on the ith mode's natural frequency is captured by the sensitivities S_{ij}, $i = 1, 2$, $j = 1, 2, 3, 4$, defined above. The rest of the parameters in (36) are given explicitly in the Appendix. Note that the coefficients η_{ii} depend linearly on the bias voltages $\hat{F}_{01}$ and $\hat{F}_{02}$. Thus, for small bias voltages, the squares of natural frequencies of oscillation around a static equilibrium change linearly with bias voltages.

D. Resonance Condition

We consider the case of resonant excitation of the second mode. The second mode can be resonantly excited when the frequency of the ac voltage at electrode 1 is near the linear natural frequency of the second mode. Further, the resonator dimensions have to be chosen such that the natural frequencies of the first and second (in-plane) resonator modes are in a $1:2$ ratio. The first- and second-mode internal resonance and the resonant actuation of the second mode are made explicit by the requirements described as follows:

$$\begin{aligned}\bar{\Omega}_1 &= \omega_{10}\,(1+\epsilon\sigma_{R2})\\ \omega_{20} &= 2\omega_{10}\,(1+\epsilon\sigma_{\rm in}).\end{aligned} \tag{41}$$

Here, $\sigma_{\rm in}$ is a detuning between the first and second natural frequencies of the nominal system, denoted by subscript "0," from perfect $1:2$ internal resonance, and σ_{R2} is the external detuning from perfect resonant excitation for the second mode.

E. Averaged Equations

The two-mode reduced-order model in (36) is nonlinear and nonautonomous. Method of averaging can be used to approximate its periodic solutions. In this method, a set of autonomous amplitude equations is obtained, which can then be studied for equilibrium solutions and their stability. We first use the method of variation of parameters to transform the equations of motion as follows:

$$\begin{aligned}a_i &= p_i\cos i\frac{\bar{\Omega}_1}{2}\tau + q_i\sin i\frac{\bar{\Omega}_1}{2}\tau\\ \dot{a}_i &= i\frac{\bar{\Omega}_1}{2}\left(-p_i\sin i\frac{\bar{\Omega}_1}{2}\tau + q_i\cos i\frac{\bar{\Omega}_1}{2}\tau\right), \qquad i=1,2.\end{aligned} \tag{42}$$

In this transformation, the variables (p_i, q_i) are functions of time. This transformation along with the resonance conditions in (41), when substituted in (36), provide a system of equations that is called in "standard form" [19], [32] for applying the method of averaging. The standard form is then averaged over the fast period to obtain slow-time equations for the variables (p_i, q_i). The resulting first-order amplitude equations are given as follows:

$$\begin{Bmatrix}\dot{p}_1\\ \dot{q}_1\\ \dot{p}_2\\ \dot{q}_2\end{Bmatrix} = \epsilon\begin{Bmatrix}-\omega_1\hat{\zeta}_1 p_1 - \omega_1(\bar{\sigma}_{R2}+\bar{\sigma}_{\rm in})q_1 + \omega_1\Lambda_1(p_1q_2 - q_1p_2)\\ -\omega_1\hat{\zeta}_1 q_1 + \omega_1(\bar{\sigma}_{R2}+\bar{\sigma}_{\rm in})p_1 - \omega_1\Lambda_1(p_1p_2 + q_1q_2)\\ -\omega_2\hat{\zeta}_2 p_2 - \omega_2\bar{\sigma}_{R2}q_2 + \frac{\omega_1}{2}\Lambda_2 p_1q_1\\ -\omega_2\hat{\zeta}_2 q_2 + \omega_2\bar{\sigma}_{R2}p_2 + \frac{\omega_1}{4}\Lambda_2\left(q_1^2 - p_1^2\right) + \frac{f_{12}\hat{F}_{11}}{4\Gamma_{22}\bar{\Omega}_1}\end{Bmatrix} \tag{43}$$

where

$$\begin{aligned}\bar{\sigma}_{R2} &= \left(\sigma_{R2} - \frac{\eta_{22}}{2\omega_2^2}\right) \quad \bar{\sigma}_{\rm in} = \left(\sigma_{\rm in} + \frac{\eta_{22}}{2\omega_2^2} - \frac{\eta_{11}}{2\omega_1^2}\right)\\ \Lambda_j &= \frac{1}{2\Gamma_{jj}}\left(\frac{Q_{10}}{2} - Q_{01}\right)|_{\epsilon=0}, \qquad j=1,2.\end{aligned} \tag{44}$$

Note that the ϵ term appearing on the right-hand side of the averaged system can be absorbed by defining a slow time scale $\epsilon\tau$. Thus, as expected, the parameters (p_1, q_1) and (p_2, q_2) are slowly varying functions of time and are asymptotic approximations to modal amplitudes a_1 and a_2, respectively. The variables $\bar{\sigma}_{R2}$ and $\bar{\sigma}_{\rm in}$ are introduced to keep equations concise and to denote effective external and internal mistunings, respectively, in the presence of variations in system parameters. The two natural frequencies of the mistuned system are related through the effective internal mistuning as follows:

$$\omega_2 = 2\omega_1(1+\epsilon\bar{\sigma}_{\rm in}). \tag{45}$$

Thus, the first and second natural frequencies of the perturbed system are in perfect internal resonance when the effective internal mistuning $\bar{\sigma}_{\rm in}$ is zero. Similarly, when the modified external mistuning $\bar{\sigma}_{R2}$ is zero, the second mode of the perturbed system is in perfect external resonance [to $O(\epsilon)$].

The averaged equations in (43) are sometimes represented in polar coordinates in terms of amplitudes B_i and phases θ_i. Assuming that $p_i = B_i\sin\theta_i$, $q_i = B_i\cos\theta_i$, $i=1,2$, the equations in (43) are transformed to the polar form as follows:

$$\begin{Bmatrix}\dot{B}_1\\ B_1\dot{\theta}_1\\ \dot{B}_2\\ B_2\dot{\theta}_2\end{Bmatrix} = \epsilon\begin{Bmatrix}-\omega_1\hat{\zeta}_1 B_1 - \omega_1\Lambda_1 B_1B_2\cos(2\theta_1-\theta_2)\\ -\omega_1(\bar{\sigma}_{R2}+\bar{\sigma}_{\rm in})B_1 + \omega_1\Lambda_1 B_1B_2\sin(2\theta_1-\theta_2)\\ -\omega_2\hat{\zeta}_2 B_2 + \frac{\omega_1}{4}\Lambda_2 B_1^2\cos(2\theta_1-\theta_2) + \frac{f_{12}\hat{F}_{11}}{4\Gamma_{22}\bar{\Omega}_1}\cos\theta_2\\ -\omega_2\bar{\sigma}_{R2}B_2 + \frac{\omega_1}{4}\Lambda_2 B_1^2\sin(2\theta_1-\theta_2) - \frac{f_{12}\hat{F}_{11}}{4\Gamma_{22}\bar{\Omega}_1}\sin\theta_2\end{Bmatrix}. \tag{46}$$

Equations in the form of the averaged equations in (43) and (46), including their equilibrium solutions and stability, have been studied in detail by many researchers (see [19, Ch. 2] for a quick overview). Note that a semitrivial steady-state equilibrium solution with a trivial (or zero) first-mode amplitude B_1 and some nonzero second-mode amplitude B_2 is a characteristic response of these equations. It is also possible to find solutions in which both B_1 and B_2 are nonzero. Such a coupled-mode response is shown to arise through a pitchfork bifurcation from the semitrivial second-mode solution when the excitation strength is increased above a threshold value. This threshold or critical value depends on other system parameters. A period-doubling route to chaos has also been observed in these systems for some parameter combinations in a lightly damped system [19], [23].

A stability analysis of semitrivial equilibrium solution [$p_1 = q_1 = 0$, and $(p_2, q_2) \neq 0$] for T-resonator averaged system provides an estimate of required threshold electrostatic force above which both the modes participate in resonator response. The resulting nondimensional electrostatic threshold force $\hat{F}_{11}$ is described as follows:

$$(\hat{F}_{11})_{\rm th} = \frac{4\bar{\Omega}_1\Gamma_{22}|_{\epsilon=0}}{f_{12}}\frac{\omega_2}{\Lambda_1}\sqrt{\left((\bar{\sigma}_{R2}+\bar{\sigma}_{\rm in})^2 + \hat{\zeta}_1^2\right)\left(\bar{\sigma}_{R2}^2 + \hat{\zeta}_2^2\right)}. \tag{47}$$

This relation shows the dependence of threshold voltage on the mistuning between the two modes and on the dissipation

in the two modes. If the two modes are perfectly tuned (i.e., $\bar{\sigma}_{\rm in} = 0$) and the system has no damping, the threshold voltage required for coupled response is zero.

It can be shown using elementary calculus that the modified external mistuning $\bar{\sigma}_{R2}$ (and thereby, the excitation frequency) for which the threshold is minimum is given by

$$\bar{\sigma}_{R2} \simeq -\frac{\hat{\zeta}_2^2}{\hat{\zeta}_1^2 + \hat{\zeta}_2^2}\bar{\sigma}_{\rm in} + O\left(\bar{\sigma}_{\rm in}^2\right). \tag{48}$$

We now have all model equations at our disposal to study the various aspects of model predictions and T-resonator response.

VII. T-Resonator Response: Numerical Results

The general formulation in the preceding nonlinear analysis allows for studying T-resonator response with tip and central masses, temperature variations and prestresses, asymmetry due to unequal lengths of beams 1 and 2, and beams with different flexural rigidities. For a given design, the natural frequencies, mode shapes, and the parameters in the averaged system can be exactly calculated. Here, we consider a specific case and revisit the T-resonator design considered in the linear analysis, with no rigid masses, zero thermal prestress, and no asymmetry (equal "bottom" beam lengths) and with all three beam segments having the same cross section and material properties. The effects of concentrated masses, asymmetries, variations in length from nominal values, and thermal stresses are presented as perturbations to the nominal system. We use beam 1 parameters for nondimensionalization. Using linear analysis results, the length ratio of the "upper" beam is set to $\nu_3 = 1.3266$ to achieve a $1:2$ internal resonance condition. In this nominal design, all three electrode gaps are assumed to be equal (i.e., $g_1 = g_2 = g_3$) and the electrode spans are set to be $\bar{l}_1 = \bar{l}_2 = \bar{l}_3 = 2/3$.

The parameters in an averaged equation for this nominal design are

$$\begin{aligned}
&\omega_1 = 1.699 && \omega_2 = 3.398\\
&\Gamma_{11} = 0.5 && \Gamma_{22} = 0.5\\
&\Lambda_1 = 0.7858 && \Lambda_2 = 0.7858 \quad \sigma_{\rm in} = 0.0001\\
&S_{11} = -4.5586 && S_{12} = -0.6074\\
&S_{13} = -5.361 && S_{14} = -0.01356\\
&S_{21} = -3.6708 && S_{22} = -9.7137\\
&S_{23} = -3.6708 && S_{24} = -0.5773\\
&\mu_{11} = 0 && \mu_{12} = -0.3006/g_1\\
&\mu_{21} = -0.057/g_1 && \mu_{22} = 0\\
&Q_{00} = 0 && Q_{10} = -0.0224\\
&Q_{02} = 0 && Q_{12} = 0\\
&f_{21} = 0.0018/g_1^2 && h_{21} = 0.9844/g_1^2\\
&f_{23} = 0.3591/g_1^2 && h_{23} = 0\\
&h_{11} = -0.8677/g_1 && h_{12} = 0 \quad f_{12} = -0.6588/g_1.
\end{aligned} \tag{49}$$

Note that the nondimensional frequencies, sensitivities, and nonlinear coupling coefficients are independent of physical dimensions and material properties. S_{ij}s are the sensitivity coefficients for the ith mode's natural frequency to variations in system parameters, as defined in (40). The electrostatic negative spring affect is captured by the coefficients (f_{21}, f_{23}) for electrode 1 and (h_{21}, h_{23}) for electrode 2. Since $h_{23} = 0$, the second mode's natural frequency remains unaffected by the bias voltage at the "upper" electrode (electrode 2). The parameters (h_{11}, h_{12}) and (f_{12}) determine the strength of electrostatic actuation in a particular mode. The nondimensional forces $\hat{F}_{11}$ and $\hat{F}_{12}$ are determined using (8) for the specified physical dimensions of the T-resonator structure. Thus, as expected, the strength of electrostatic actuation in comparison to structural elastic energy is dependent on the actual length scale.

A. Approximate Nondimensional Pull-In Force

The nondimensional quantities specified so far are independent of the dimensions of the device. However, structural cubic nonlinearities in the equations governing pull-in voltages, i.e., (31) and the definition of cubic terms in the Appendix, depend on the ratio of beam thickness to length (parameters κ_i, $i = 1, 2, 3$). The intent in this section is to provide simple analytical formulas for pull-in voltages that are valid for any nominal T-resonator design and, as a result, consider static equilibrium equations [see (31)] with only linear structural terms in deriving formulas here. The effect of cubic stretching and curvature nonlinearities will be included in calculating the pull-in voltages when the response of a T-resonator with a specific dimension is considered. However, in general, it can be expected that the pull-in voltages will be higher when stretching nonlinearities are included. Thus, the formulas here will provide a lower estimate of pull-in voltages.

The pull-in voltages are obtained for each electrode individually; for example, when considering the pull-in voltage for electrode 1, only the bias voltage on electrode 1 is assumed. Note that when the bias voltage is applied on electrode 1, the first mode does not participate in the response. When the voltage is applied on electrode 2, the modal participation of the second mode can be assumed to be very small as the "bottom" beams deflect symmetrically in the second mode while the response caused by the force of electrode 2 is asymmetric. Thus, the participation of the second mode is neglected in calculating the pull-in voltage for electrode 2.

Fig. 5(a) and (b) shows the static deflections A_{10}/g_1 and A_{20}/g_3 as functions of electrostatic voltages represented by nondimensional ratios F_{01}/g_1^2 and F_{02}/g_3^2, respectively. Since the equilibrium equations are nonlinear, these plots show multiple equilibrium deflections for some electrostatic forces. Physically, when the electrostatic forces are small and are slowly increased starting from zero, the deflections follow the upper branch close to zero equilibrium. The pull-in forces can be obtained from the plots by identifying the ratio at which the two solution branches merge or the slope of the solution curve is ∞. The pull-in nondimensional forces thus obtained by considering linear stiffness and up to tenth-order electrostatic terms (to achieve convergence) are

$$\frac{F_{01}}{g_1^2} = 4.58 \quad \frac{F_{02}}{g_3^2} = 0.41. \tag{50}$$

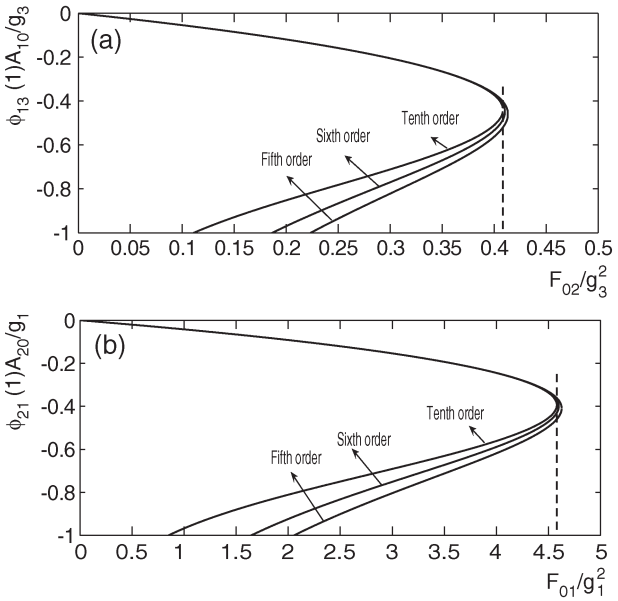

Fig. 5. Nondimensional deflections for the T-resonator structure as a function of electrostatic forces. (a) Ratio of the maximum "upper" beam deflection to the "upper" electrode gap as a function of "upper" electrode force. (b) Ratio of the maximum "bottom" beam deflection to the "bottom" electrode gap as a function of "bottom" electrode force.

B. Periodic Response of a T-Resonator

Now, we present periodic response results for the nominal T-resonator. We assume both electrode gaps d_1 and d_3 to be 2 μm. The "upper" beam length L_3 is set to 133 μm for nominal design. Note that this deviates from the ideal length ratio of $L_3 = 1.3266L_1$ and, thus, acknowledges fabrication uncertainties. The resonator is consequently slightly mistuned from 1 : 2 internal resonance, and the mistuning is determined by the sensitivities S_{11} and S_{21} [see (40)] associated with the "upper" beam length mistuning σ_{L_3}. The resulting decrease in the first and second natural frequencies due to the presence of this length mistuning are 0.08% and 0.40%, respectively. The effective internal mistuning from 1 : 2 internal resonance [see (45)] for the nominal design with zero bias voltages is $\bar{\sigma}_{\rm in} = 0.0033$ (or 0.33%).

Bias voltages are first set such that the effective internal mistuning from 1 : 2 internal resonance reduces to zero. Further, the bias voltages must be much smaller than the pull-in voltages to avoid static or dynamic pull-in instability [27], [33]. Using the results in (50), we get $V_{b1} = 177$ V and $V_{b2} = 53$ V for the electrodes 1 and 2 pull-in voltages, respectively. Pull-in voltages when calculated specifically for this resonator dimensions and properties using a model that includes up to cubic stiffness terms (as compared to only linear stiffness terms) are $V_{b1} = 182$ V and $V_{b2} = 53$ V. Thus, the electrode 1 pull-in voltage shows a small increase when cubic stiffness terms are included; however, the electrode 2 pull-in voltage remains essentially unchanged. Note that for electrode 1 pull-in, cubic nonlinearities are due to the stretching of the midplane, which are significant even for small deflections; for electrode 2 pull-in, however, the cubic nonlinearities are due to the curvature of the beam deflection, which become significant only at much larger beam deflections. The static deflection of the T-structure with the bias voltage on electrode 1 is essentially that of a fixed–fixed beam with a distributed load. Thus, the pull-in voltage obtained in this study for electrode 1 is compared to the pull-in voltage obtained by using the formulas by Pamidighantam *et al.* [27] for fixed–fixed beams. Note that in [27], the approximate formulas developed for pull-in voltages were verified to be in very good agreement with simulation results from the finite-element MEMS software CoventorWare. In using the formulas, the effective stiffness of the structure is calculated for the electrode length used in this paper, and the maximum deflection of the beam—needed for calculating stiffening effect due to beam deflection—is assumed to be one-third of the electrode gap, which is the first-order approximation for pull-in voltage deflection. The effective width of the beam is adjusted for fringe voltage effects. The pull-in voltage thus obtained for electrode 1 from the formulas in [27] is 165 V. However, when the fringe field effect is not included and the effective width is assumed to be the same as the width of the beam, the resulting pull-in voltage is 178 V. We also note that the pull-in voltage (without fringe effects) varies from 176 to 182 V when the assumed maximum deflection to the electrode gap ratio is varied from 0.2 to 0.5, respectively. These results are in very good agreement with the pull-in voltages obtained in this study for electrode 1.

The effective internal mistuning, as defined in (45), decreases (increases) as the bias voltage at electrode 1 (2) increases. We set the bias voltages to $V_{b1} = 32$ V and $V_{b2} = 5$ V, which results in a decrease in the internal mistuning of the resonator from 0.33% (with no bias voltages) to less than 0.004%. We assume a quality factor $Q = 5000$ ($\zeta_1 = \zeta_2 = 0.001$) for each of the two modes, which is a reasonable assumption for microresonators operating in vacuum [34]. Nondimensional scaling parameter ϵ is set to 1 for the results in this section. The equilibrium solutions of averaged system in (43) are obtained through the bifurcation and continuation software AUTO [35] and are shown in Fig. 6(a) and (b). Fig. 6(a) shows the transverse displacement of the "upper" beam tip as a function of the actuation signal frequency for different values of the ac voltage $V_{\rm ac}$. Fig. 6(b) shows the corresponding transverse displacement of beams at the junction of the three beams.

As already indicated earlier, there are two types of solutions. The semitrivial solution is the one in which B_1 is zero and B_2 is nonzero. Thus, this solution is the resonant response of the second mode and exists for all applied voltages $V_{b1}V_{\rm ac} \neq 0$ over the entire frequency interval with a peak near 396.75 kHz. In this response, the upper beam has no transverse displacement, and only the bottom beams move, as shown in Fig. 6(b). The second type of solutions are those in which both B_1 (or a_1) and B_2 (or a_2) are nonzero. This solution branch arises through a pitchfork bifurcation instability of the semitrivial branch only when $V_{\rm ac}$ is taken such that the threshold voltage is exceeded. The threshold voltage for this resonator, using (47), is $V_{b1}V_{\rm ac} = 0.08$ V^2. Thus, when the applied ac voltage exceeds the threshold, the response of "bottom" beams (the semitrivial response of the resonator) becomes unstable [indicated by the dotted lines in Fig. 6(b)] and a new stable coupled-mode response arises due to a pitchfork bifurcation, as visible in Fig. 6(a) for the "upper" beam response. Note that in this nonlinear interaction between the two flexural modes, the first mode

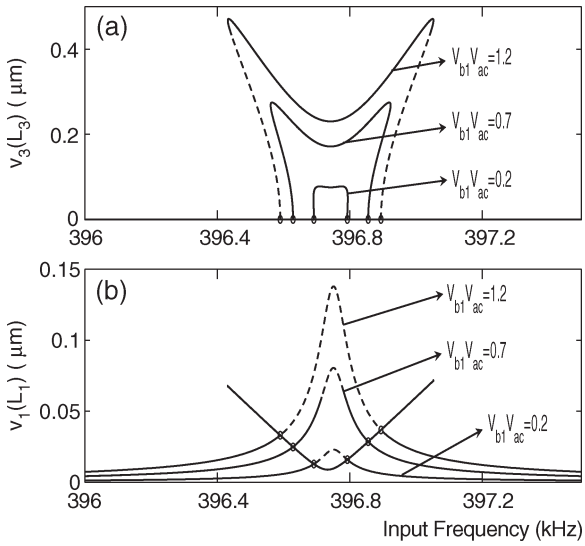

Fig. 6. Response of a T-resonator when excited resonantly in the second mode as a function of input frequency for different ac voltages ($V_{b1}V_{\rm ac}$ in square volts, with $V_{b1} = 32$ V). The response is obtained through averaged equations. (a) "Upper" beam's tip response. (b) "Bottom" beams' transverse displacement at the junction. Parameters for the microresonator are given as follows: $L_1 = L_2 = 100\ \mu$m; $L_3 = 133\ \mu$m; $t_1 = t_2 = t_3 = 3\ \mu$m; $b_1 = b_2 = b_3 = 5\ \mu$m; $d_1 = d_3 = 2\ \mu$m; $V_{b2} = 5$ V; $\zeta_1 = \zeta_2 = 0.0001$; $E_1 = 169$ GPa; and $\rho = 2330$ kg/m^3. Solid lines represent stable responses, and dotted lines represent unstable responses.

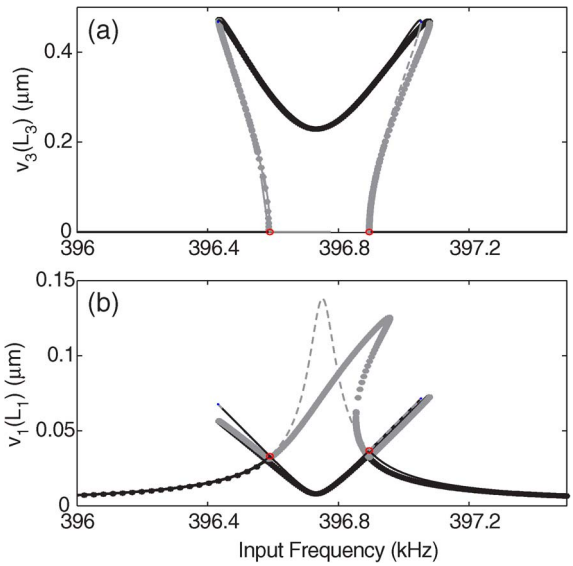

Fig. 7. Microresonator response as a function of input frequency for ac voltage $V_{\rm ac} = 1.2/V_{b1}$ V. Lines with marker "$*$" denote periodic solutions constructed through AUTO using the two-mode model that includes cubic structural and up to fifth-order actuation nonlinearities. Lines with no marker denote averaged system predictions. (a) "Upper" beam's tip response. (b) "Bottom" beams' transverse displacement at the junction. Parameters of the microresonator are given as follows: $L_1 = L_2 = 100\ \mu$m; $L_3 = 133\ \mu$m; $t_1 = t_2 = t_3 = 3\ \mu$m; $b_1 = b_2 = b_3 = 5\ \mu$m; $d_1 = d_3 = 2\ \mu$m; $V_{b1} = 32$ V; $V_{b2} = 5$ V; $\zeta_1 = \zeta_2 = 0.0001$; $E_1 = 169$ GPa; and $\rho = 2330$ kg/m^3. Solid lines represent stable responses, and dotted lines represent unstable responses.

causes the "upper" beam to oscillate with nonzero transverse displacement at half the input frequency [see (42)]. In addition, the directly excited second mode has its amplitude drastically reduced in this coupled mode as compared to the case when the motion is in a semitrivial solution branch. Thus, the "upper" beam response v_3 is nonzero only over a small frequency interval around the directly excited resonant frequency.

The frequency bandwidth over which the first mode response exists depends on the actual voltage $V_{b1}V_{\rm ac}$ above the threshold voltage. Therefore, although the coupled-mode response starts to exist for a very small threshold voltage, for a practical range of frequencies, the actual voltage must be much higher than the threshold voltage. Furthermore, observe that the frequency bandwidth over which the "upper" beam responds can be adjusted by changing the ac voltage level, even if the maximum ac voltage is limited by possibility of dynamic pull-in [33].

The periodic solutions of the two-mode model equations of motion [see (36)] that include cubic structural nonlinearities and up to fifth-order electrostatic actuation nonlinearities with ac voltage $V_{\rm ac} = 1.2/V_{b1}$ are computed numerically using the software AUTO, and the results obtained by this higher order (and fidelity) nonlinear model are shown in Fig. 7(a) and (b). Here, we take advantage of the fact that the time-dependent model can be appropriately formulated in AUTO to numerically find its periodic solutions, as opposed to the equilibrium solutions of the averaged system, which can be obtained analytically. The approximate response obtained using averaged system is also shown in the same figure. In the response of "bottom" beam shown in Fig. 7(b), the hardening nonlinearity due to stretching is clearly visible; however, the nonlinearities have little effect on the response arising due to modal interaction between the two modes. Note that the stable response amplitude of "bottom" beam is much smaller than the unstable response, which represents the response of the mode in the absence of modal interaction. Fig. 7(a) shows that the averaged system response for the "upper" beam using only up to quadratic nonlinearities matches very well with the model that includes higher order nonlinearities. Furthermore, averaging provides a very good approximation of the response exhibited by the two-mode model.

C. *Effect of Damping*

The threshold actuation level [see (47)] required to indirectly excite the "upper" beam is strongly dependent on system damping and mistunings. The effects of damping in general on a two-degree-of-freedom autoparametric system are detailed in [19] and [23]. Interestingly, the emergence of Hopf bifurcation in an autoparametric system is also strongly dependent on internal mistuning and modal dampings. For a given excitation level, a decrease in damping in the two modes accompanied with mistuning from exact $1:2$ internal resonance can result in a Hopf bifurcation followed by a period-doubling bifurcation route to chaos for certain parameter combinations [23].

In Fig. 8, the resonator response is shown for modes with lower quality factors, i.e., $Q = 500$. The quality factor of $Q = 500$ corresponds to modal dampings $\zeta_1 = \zeta_2 = 0.001$. The bias voltages and other parameters, except for damping, remain unchanged from the parameters used for Fig. 6. A tenfold increase in damping results in an increase in the threshold actuation by a hundred times to $V_{b1}V_{\rm ac} = 8\ ({\rm V})^2$. Thus, as the damping increases, the minimum voltage required to indirectly excite the "upper" beam increases considerably. Note, however,

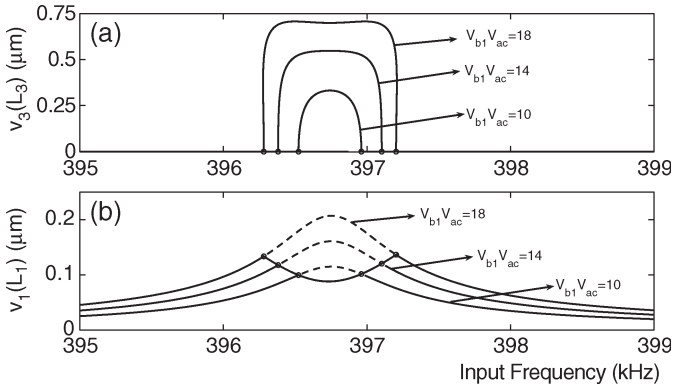

Fig. 8. Response of the T-resonator for increased dampings $\zeta_1 = \zeta_2 = 0.001$ as a function of input frequency for different actuation voltages $V_{\rm ac}$ (in volts). (a) "Upper" beam's tip response. (b) "Bottom" beams' transverse displacement at the junction. Parameters of the microresonator are given as follows: $L_1 = L_2 = 100\ \mu$m; $L_3 = 133\ \mu$m; $t_1 = t_2 = t_3 = 3\ \mu$m; $b_1 = b_2 = b_3 = 5\ \mu$m; $d_1 = d_3 = 2\ \mu$m; $V_{b1} = 32$ V; $V_{b2} = 5$ V; $E_1 = 169$ GPa; and $\rho = 2330$ kg/m^3. Solid lines represent stable responses, and dotted lines represent unstable responses.

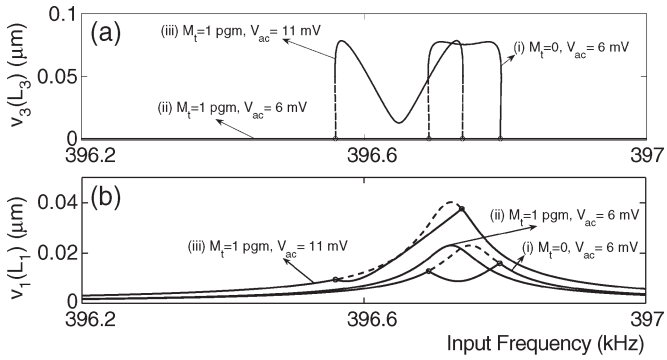

Fig. 9. Response of the T-resonator as a function input frequency for (i) zero added mass and ac voltage $V_{\rm ac} = 6$ mV, (ii) an added mass of 1 pg at the "upper" beam tip, with $V_{\rm ac} = 6$ mV, and (iii) an added mass of 1 pg at the "upper" beam tip, with $V_{\rm ac} = 11$ mV. Parameters of the microresonator are given as follows: $L_1 = L_2 = 100\ \mu$m; $L_3 = 133\ \mu$m; $t_1 = t_2 = t_3 = 3\ \mu$m; $b_1 = b_2 = b_3 = 5\ \mu$m; $d_1 = d_3 = 2\ \mu$m; $V_{b1} = 32$ V; $V_{b2} = 5$ V; $\zeta_1 = \zeta_2 = 0.0001$; $E_1 = 169$ GPa; and $\rho = 2330$ kg/m^3. Solid lines represent stable response, and dotted lines represent unstable response.

that when excited, the upper beam's response is nearly constant over the whole interval of existence. Thus, the response output of the upper beam is very sensitive to changes in excitation frequency as well as minimum voltages applied to the actuating electrode.

Now that we have described the basic operation of the T-resonator, we present the effects of adding mass and changes in the dimensions of the beams forming the resonator.

D. Effects of Adding a Tip Mass

A mass particle when placed on the "upper" beam tip changes the natural frequencies and internal mistuning of the interacting modes, as predicted by (39), (44), and (45). The change in internal mistuning is directly proportional to the mass ratio R_t, and thus, the resonator will be tuned toward or away from $1:2$ internal resonance by the addition of a tip mass. Also note that for a given tip mass, the change in natural frequencies and internal mistuning will be larger for a smaller structure due to a bigger mass ratio R_t.

Measurement of resonance frequency shift on addition of a mass particle is the basis of many MEMS mass sensors. Detection up to subattogram mass measurements has been reported using a resonantly excited nanosized cantilever structure [36], [37]. In the microresonator regime, with structure thickness, width, and length in micrometers, subpicogram measurements have been reported [3], [20].

Fig. 9 illustrates the effect of adding a picogram mass on the "upper" beam tip in a typical T-resonator. We assume a quality factor of 5000 for each of the modes. Except for the ac voltage and the added mass, all other parameters are the same as for Fig. 6. Response curves are shown for the following three different ac voltages: 1) without any tip mass, and $V_{\rm ac} = 6$ mV; 2) with a tip mass of 1 pg, and $V_{\rm ac} = 6$ mV; and 3) with a tip mass of 1 pg, and $V_{\rm ac} = 11$ mV. The "upper" beam tip oscillation amplitude is $\sim 0.08\ \mu$m at half the input frequency for case 1), i.e., when there is no tip mass. When a tip mass of 1 pg is placed on the upper beam [case 2)], the two modes are sufficiently mistuned away so that the first mode is not excited. Thus, the "upper" beam oscillation amplitude goes down to zero. Increasing the voltage to $V_{\rm ac} = 11$ mV [case 3)] resets the maximum tip amplitude of the "upper" beam to $\sim 0.08\ \mu$m. Thus, not only is there a frequency shift, but the nonlinearly excited response of the "upper" beam is also so sensitive to mass perturbation that it can switch from nonzero to zero due to the addition of a small mass. This response can, again, be restored with an increase in the ac voltage. Thus, a shift in the ac voltage level instead of the resonance frequency is another possible measure that can be used for mass sensing with the nonlinear T-resonator. These results suggest that there is promise in working toward possible application for T-resonator as a mass sensor and is a topic of further research.

E. Effect of Length Mistuning

The effect of changing the "upper" beam's length on natural frequencies is captured by sensitivities S_{i1}, with $i = 1, 2$, for length change ratio σ_{L3} in (39), (44), and (45). The effective internal mistuning, as defined in (45), is increased by increasing the length of "upper" beam and vice versa. Thus, the effect of the "upper" beam length change is similar to the effect of adding a tip mass at the "upper" beam.

When the two "bottom" beams have unequal lengths, the result is a nonzero mistuning σ_{L2}, as defined in (35). The sensitivities S_{i2}, $i = 1, 2$, in (49) for the mistuning σ_{L2} were obtained using the mode shapes of the symmetric nominal system. We note that a resonator structure with unequal "bottom" beam lengths is no longer symmetric, and thus, the "upper" beam has a nonzero displacement component in the second mode of the T-resonator. For the example resonator considered here, a change in length of beam 2 from 100 to 101 μm, keeping all other parameters the same as the nominal system, results in changing the effective internal mistuning in (45) from 0.33% to -0.29% for zero bias voltages. The change in internal mistuning is calculated by using the sensitivities S_{i2} in (49). To tune the system to exact $1:2$ internal resonance, the bias

voltages are set to $V_{b1} = 21$ V and $V_{b2} = 10$ V, which results in reducing the mistuning to 0.004%.

Note that the two-mode model of the system with unequal lengths for beams 1 and 2 could be redeveloped based on the methodology for linear analysis already presented earlier. This will give a more accurate model without the assumption of symmetric second mode for the nominal system. If this approach is followed, the two-mode model predicts a -0.36% effective internal mistuning with zero bias voltages. The nonlinear coefficients also change, though by only less than 0.5% from the nominal system parameters to $\Lambda_1 = \Lambda_2 = 0.7823$. The effective internal mistuning reduces to -0.002% when the bias voltages are set to $V_{b1} = 18$ V and $V_{b2} = 10$ V. More important from the point of operation of the resonator, the "upper" beam has a small nonzero transverse deflection (approximately one-hundredth of the beam 1 deflection at the junction) in the second mode. Thus, in a semitrivial solution, the "upper" beam oscillates with a small amplitude at the input frequency due to direct excitation; however, the nonlinear response after pitchfork bifurcation is quite distinct due to its larger amplitude response with oscillations at half the input frequency.

F. Effect of Residual Stresses

Residual stresses in a microresonator are known to depend primarily on the fabrication process and choice of material for the resonator. Surface micromachined polysilicon resonators can have significant residual stresses, resulting in large variations in the resonator natural frequencies [38]. Data published by MEMSCAP Inc. [39] for the last 20 runs of the polySilicon Multi User MEMS Processes (poly-MUMPS) process (from run 61 to 81) show that the maximum residual stress in the structural polysilicon layer is 15 MPa in compression, with average stress and standard deviation of 7.6 MPa (compression) and 3 MPa, respectively. The maximum residual stress for the ground electrode polysilicon layer (for runs 61 to 81) is reported as 41 MPa (compression), with average stress and standard deviation of 25.5 MPa (compression) and 7.6 MPa, respectively.

Using the sensitivities S_{i4}, $i = 1, 2$, for residual stress mistuning $\hat{S}_T$, the effect of residual stresses on natural frequencies and effective internal mistuning in (45) can be computed. The dependence of internal mistuning $\bar{\sigma}_{\text{in}}$ can be traced to the coefficients η_{11} and η_{22} in (44), and further to the expressions in (39). For small changes, it can be seen that the coefficients η_{11} and η_{22} depend linearly on the residual stress parameter $\hat{S}_T$, which is directly proportional to the thermal strain equation in (25). Thus, the internal mistuning is linearly proportional to the residual thermal strain for small strains. For example, a compressive stress of 20 MPa in the "bottom" beams changes the effective internal resonance mistuning $\bar{\sigma}_{\text{in}}$ to -6.8% with zero bias voltages. Since the bias voltages need to be kept small to avoid pull-in instabilities, reducing the internal mistuning by adjusting bias voltages is not a good choice in this case. However, if the "upper" beam length is increased to $L_3 = 140$ μm, the effective internal mistuning [see (45)] reduces to -0.2% for zero bias voltages. The mistuning can be reduced further to less than -0.01% by setting the bias voltages to $V_{b1} = 28$ V and $V_{b2} = 10$ V. We note that the Euler buckling stress for the bottom beam for this example resonator is nearly 125 MPa.

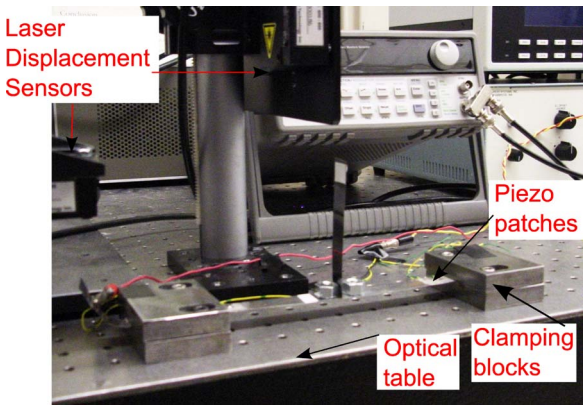

Fig. 10. Macroscale T-structure used in the experiments.

The two-mode model for the system with a compressive residual stress of 20 MPa in the bottom beams is redeveloped using the analysis procedure described for the nominal system. The new model that directly accounts for the compressive stress of 20 MPa predicts effective internal mistuning, with zero bias voltages, to be -7.1% when the length of the "upper" beam is assumed to be 133 μm. To obtain the new design length of the "upper" beam, the natural frequencies of the system with 20 MPa compressive stress are obtained analytically for different "upper" beam lengths in steps of 1 μm. The analysis predicts that the effective internal mistuning, with zero bias voltages, reduces to a minimum of 0.4% for the "upper" beam length of $L_3 = 140$ μm. Note that in the present case of a T-resonator with 20 MPa compressive stress, the design length of the "upper" beam, i.e., $L_3 = 140$ μm, predicted by the model that directly accounts for the residual stress, remains the same as that obtained by using the residual stress sensitivities S_{i4}, $i = 1, 2$, for a nominal system with no residual stress.

VIII. Experimental Results

In this section, we describe a macroscale T-beam structure and present a sample set of experimental response results to qualitatively validate the concept of the T-resonator. Details of this experimental investigation can be found in [40].

A photograph of the T-beam structure is shown in Fig. 10. The structure is formed by two strips of stainless-steel shim that are cut and glued to each other to form an upside down T. The lower or the horizontal beam is clamped at its ends. The clamped boundary conditions are achieved by holding the bottom beam between two large steel blocks at each end. The lengths of the right and left segments of the bottom beam are denoted, respectively, by L_1 and L_2. The length of the upper beam is denoted by L_3. The thickness and width of the beams are denoted by t_b and w_b, respectively. Two masses are placed on the bottom beam near the T-junction, and a small mass is attached to the vertical beam near its tip. These were necessary to assure that the structure was tuned to achieve the required 1 : 2 resonance between the two desired modes. Details of this tuning process can be found in [40]. Piezoelectric ceramic patches in the form of thin strips are bonded to the

TABLE I
DIMENSIONS AND PROPERTIES OF THE TUNED T-BEAM STRUCTURE AND PIEZO PATCHES

Property	Value
Beams	
Material	Stainless steel
Beam Lengths L_1, L_2, L_3	8.9, 8.9, 9.2 cm
Beam width w_b	1.8 cm
Beam thickness t_b	0.018 cm
Mass on the bottom beams M_c	14 gm
Mass on the upper beam M_t	0.2 gm
Upper beam mass location l_u	8.7 cm
Piezo Patches	
Material	Piezoelectric sheet (Item no. PSI-5H-4E from Piezo Systems, Inc.)
Length L_p	1.90 cm
Width w_p	1.5 cm
Thickness t_p	0.0075 in (0.01905 cm)

bottom beams on both the lower and upper surfaces near the two clamped ends. The length, thickness and width of the piezo patches are denoted by L_p, t_p, and w_p, respectively. When a voltage is applied to a piezo patch glued to a beam, a bending moment is induced, which excites the beam structure. The dimensions and properties of the T-structure and the piezo patches used for the results presented in this paper are listed in Table I. These dimensions and masses are for the T-structure that has been tuned to have the first and the second modes in 1 : 2 resonance.

Now that we have described the T-structure and the piezo patches for exciting the structure, we describe the experimental setup. The experimental setup to conduct experiments and to measure the response consists of the following: 1) a T-beam structure with piezo patches and with two ends clamped; 2) two laser displacement sensors to measure the displacements of the upper beam and one of the bottom beams; 3) a function generator to provide harmonic and sweep signals; 4) a piezo amplifier; and 5) a National Instrument data acquisition card with signal conditioner. A block diagram of the setup is shown in Fig. 11. The response of the T-structure due to piezo actuation is measured by laser displacement sensors and recorded using the data acquisition card connected to a computer. The sensor measuring displacement of a point on the upper beam as well as its output are referred to as LD1, while the sensor measuring the displacement of a point on the bottom beam as well as the output are referred to as LD2.

Different sets of experiments were conducted with the T-structure. In the first set of experiments, impulse responses of the T-structure obtained by impacting the upper and the bottom beams were captured. These were used to estimate the natural frequencies and damping factors for the two interacting modes. The linear natural frequencies for the first and second modes of the T-structure were estimated to be 14.81 Hz and between 29.65 and 29.75 Hz, respectively.

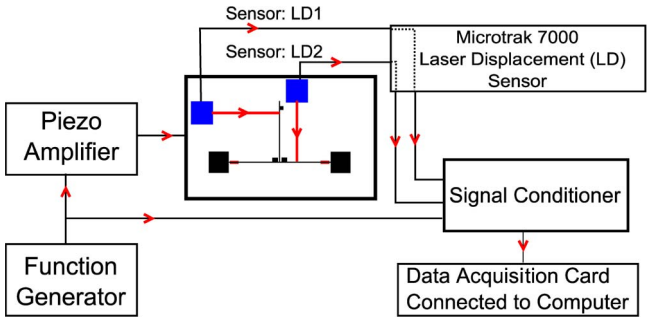

Fig. 11. Block diagram of the experimental setup for exciting a T-beam structure and measuring its response.

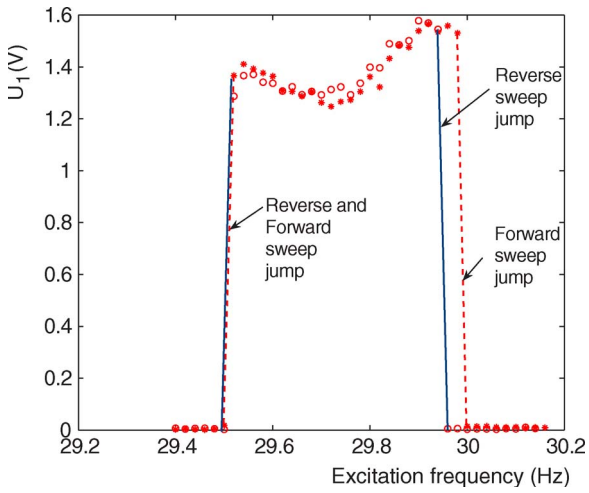

Fig. 12. Frequency–amplitude response curve of the tuned T-structure in the first mode U_1 as a function of excitation frequency. This response component is at half the excitation frequency. (∗) Forward sweep. (○) Reverse sweep. Excitation and measurement parameters are given as follows: excitation amplitude, 1 V; sampling rate, 300 Hz; samples, 9000; and amplifier gain. 20. Excitation frequency is varied quasi-statically in steps of 0.02 Hz.

In the second set, steady-state responses of the tuned T-structure were recorded when the excitation frequency applied to the piezo patches was changed quasi-statically in steps of 0.02 Hz around 29.62 Hz, which is twice the first mode's natural frequency. The amplitude of excitation was kept constant at 1 V. When the excitation frequency was changed, the response was allowed to reach a steady state before taking any measurements. The LD1 and LD2 data were recorded for 30 s at a sampling frequency of 300 Hz at each frequency step. The frequency components of the response at the excitation frequency and at half the excitation frequency were computed using a fast Fourier transform (FFT) and interpolation. The response amplitudes thus obtained at half the excitation frequency using FFTs of the LD1 and LD2 data are referred to as the first mode response (or the contribution from first mode) and are denoted by U_1 and B_1, respectively. The response component at the excitation frequency using FFTs of LD1 and LD2 data are referred to as the second mode response and are denoted by U_2 and B_2, respectively. Fig. 12 shows the first mode response U_1 (using LD1 data) as a function of the excitation frequency. Fig. 13 shows the corresponding response U_2, which is for the second mode. In both figures, forward sweep is shown by marker "∗," and reverse sweep is shown by marker "○."

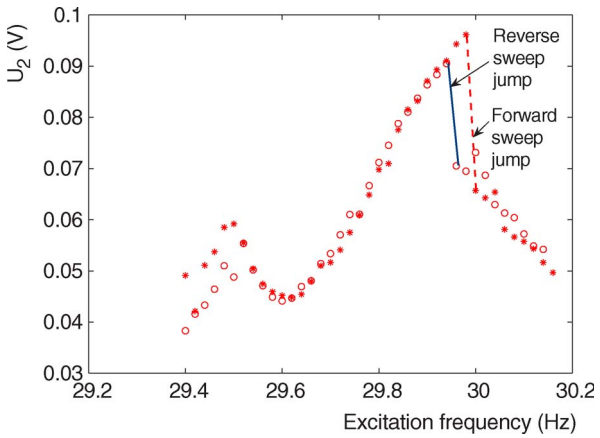

Fig. 13. Frequency–amplitude response curve of the tuned T-structure in the second mode U_2 as a function of excitation frequency. This response component is at the excitation frequency. (∗) Forward sweep. (○) Reverse sweep. Parameters for measurement and excitation are given as follows: excitation amplitude, 1 V; sampling rate, 300 Hz; samples, 9000; and amplifier gain, 20. Excitation frequency is varied quasi-statically in steps of 0.02 Hz.

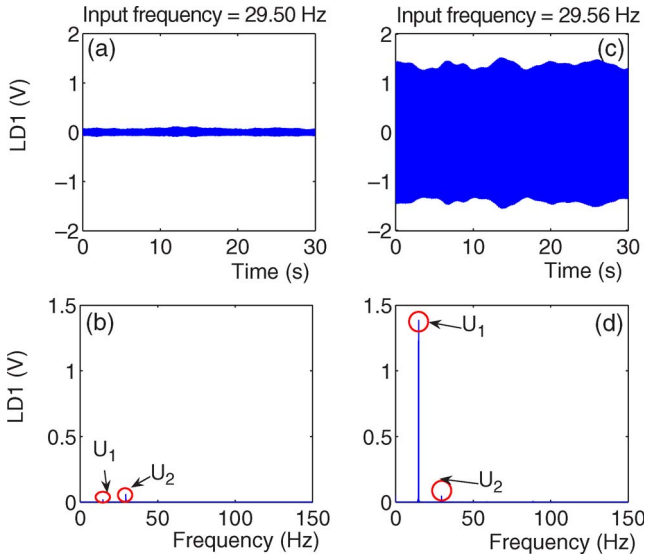

Fig. 14. Steady-state time response of the tuned T-structure measured by sensor LD1 for two excitation frequencies: (a) 29.50 Hz and (c) 29.56 Hz. The corresponding FFTs are shown in (b) and (d), respectively. Excitation and measurement parameters are given as follows: excitation amplitude, 1 V; sampling rate, 300 Hz; samples, 9000; and amplifier gain, 20.

When the structure is excited at the frequency of 29.4 Hz, only the second mode contributes to the response, and the first mode response (U_1 in Fig. 12) is zero. As the frequency is increased (forward sweep) in small steps, the amplitude of the first mode remains almost zero before it gets autoparametrically excited at 29.52 Hz, and its amplitude shows a big jump to 1.4 V (this corresponds to 3.5 mm of upper beam tip displacement) from below 0.02 V. Upon further increasing the excitation frequency, the first mode response does not show much change until 29.98 Hz when it jumps again to below 2 mV in a frequency step change of 0.02 Hz. The second mode response in Fig. 13 first decreases and then increases and also shows a jump in amplitude between 29.98 and 30.0 Hz. Fig. 14(a) and (c) shows the steady-state time response measured by sensor LD1 at excitation frequencies of 29.50 and 29.56 Hz, respectively. The corresponding FFTs computed using MATLAB are shown in Fig. 14(b) and (d), respectively. Here, the associated first mode component U_1 and the second mode component U_2 are also shown. The time histories and FFTs show a clear change in the upper beam response amplitude.

When the frequency is decreased from 30.16 Hz (reverse sweep), the first mode response amplitude remains less than 0.02 V for excitation frequencies below 29.98 Hz and jumps to a large amplitude at an excitation frequency of 29.94 Hz. Thus, the response shows hysteresis in the forward and reverse sweeps. These characteristics are typical of the T-resonator responses presented in Section VII (see Figs. 6 and 7). The first mode response having nonzero amplitude only in a narrow frequency bandwidth and at a frequency half the excitation frequency forms the basis of proposing the T-resonator for RF MEMS filter–mixer applications. These results validate, at least qualitatively, the analytical predictions made through analysis of the T-resonator.

IX. Summary and Conclusion

In this paper, a novel T-beam microresonator structure that works on the principle of nonlinear modal interactions due to 1 : 2 internal resonance has been introduced. The microresonator is designed such that the lowest two flexural mode's natural frequencies are in a 1 : 2 ratio. Though linearly uncoupled, the two modes are nonlinearly coupled through inertial nonlinearities. The response of this nonlinear microresonator has the following unique characteristics in comparison to a typical linear microresonator: 1) The directly excited higher flexural mode, when driven above a threshold actuation voltage, excites the internally resonant lower frequency flexural mode due to autoparametric instability phenomenon; 2) the frequency bandwidth over which the lower frequency mode participates in the response can be controlled by actuation voltage; 3) the nonlinearly excited lower mode results in the T-beam resonator response output at half the input frequency; and 4) the response component at half the input frequency is nonzero only when the input frequency is close to the natural frequency of the directly excited higher frequency flexural mode. Thus, the resonator response in lower flexural mode acts as a filter, with very high out-of-band rejection, that only allows input frequencies close to the higher frequency flexural mode. In addition, the T-beam microresonator can also perform mixing operation as the microresonator output response is at half the input frequency. The dependence of bandwidth on actuation in a nonlinear T-beam microresonator can be potentially used in designing voltage-controllable bandwidth filter devices.

The effect of various perturbations on resonator natural frequencies and nonlinear responses are considered, and it is shown that the resonator is very sensitive to changes from the nominal design. It is illustrated that voltage tuning can be used to tune the resonator natural frequencies in 1 : 2 internal resonance, and in some cases, postfabrication treatment may be required to tune the resonator modes to 1 : 2 internal resonance. The high sensitivity of the resonator to perturbations can also be utilized to design a very effective sensor. The simulations show that the resonator response amplitude at half the input

frequency, with the lower mode component arising due to nonlinearities, can drastically change and even be eliminated when a small mass (less than 0.01% of the mass of the microresonator) is placed on the resonator. The nonlinear response can be then reactivated by increasing the voltage level. Thus, the required increase in voltage level can serve as a measure for the added mass. Note that as the quality factor decreases, the threshold voltage required for indirectly exciting the lower mode increases considerably. Consequently, power handling, in addition to thermal stability, can be critical to the performance of this resonator as an RF filter and mass sensor. Finally, results of macroscale experiments are shown to qualitatively validate the T-resonator proposed here.

APPENDIX

Here, variables introduced in the two-mode system Lagrangian in (30) are defined. Kinetic and potential energy coefficients $(\Gamma_{11}, \Gamma_{12}, \Gamma_{22})$ and (W_{11}, W_{12}, W_{22}) associated with linear terms in equations of motion are given as follows:

$$\begin{aligned}\Gamma_{ij} = &\left(\frac{1}{2}\sum_{k=1}^{3} r_k \nu_k \int_0^1 \phi_{ik}\phi_{jk} d\bar{s}_k\right) \\ &+ \frac{1}{2}\frac{\gamma_c}{\nu_1^2}\phi'_{i1}\phi'_{j1}\bigg|_{\bar{s}_1=1} + \frac{\gamma_t}{\nu_3^2}\phi'_{i3}\phi'_{j3}\bigg|_{\bar{s}_3=1} \\ &+ \frac{1}{2}\left(r_3\nu_3(1+R_t) + R_c(r_1\nu_1 + r_2\nu_2)\right)\phi_{i1}\phi_{j1}\bigg|_{\bar{s}_1=1} \\ &+ \frac{\gamma_t}{\nu_3^2}\phi'_{i3}\phi'_{j3}\bigg|_{\bar{s}_3=1} + \frac{1}{2}R_t r_3 \nu_3 \phi_{i3}\phi_{j3}\bigg|_{\bar{s}_3=1} \end{aligned} \tag{A1}$$

$$\begin{aligned}W_{ij} = \frac{1}{2}\Bigg(&\left(\sum_{k=1}^{3}\frac{\alpha_k}{\nu_k^3}\int_0^1 \phi''_{ik}\phi''_{jk}d\bar{s}_k\right) \\ &- \left(\sum_{k=1}^{2}\frac{S_T}{\nu_k}\int_0^1 \phi'_{ik}\phi'_{jk}d\bar{s}_k\right)\Bigg).\end{aligned} \tag{A2}$$

To concisely write coefficients Q_{ij}, Θ_{ij}, and K_i in (30), we first write a two-mode approximation for axial displacements using (10) and (13) as follows:

$$\hat{u}_k = \chi_{11k}\, A_1^2 + \chi_{22k}\, A_2^2 + 2\chi_{12k}\, A_1 A_2 \tag{A3}$$

where $k = 1, 2, 3$, and variables χ_{ijk} are spatial functions of nondimensional arc length $\bar{s}_k$, described as follows:

$$\left.\begin{aligned}\chi_{ijk} = &\tfrac{1}{2}\tfrac{\nu_k}{\nu_1+\nu_2}\bar{s}_k\left(\sum_{m=1}^{2}\tfrac{1}{\nu_m}\int_0^1 \phi'_{im}\phi'_{jm}d\bar{s}_m\right) \\ &- \tfrac{1}{2}\tfrac{1}{\nu_k}\int_0^{\bar{s}_k}\phi'_{ik}\phi'_{jk}d\bar{s}_k, \qquad k = 1,2 \\ \chi_{ij3} = &-\tfrac{1}{2}\tfrac{1}{\nu_3}\int_0^{\bar{s}_3}\phi'_{i3}\phi'_{j3}d\bar{s}_3.\end{aligned}\right\} \tag{A4}$$

Coefficients Q_{ij} are then defined as follows:

$$Q_{ij} = R_t r_3 \nu_3 \bar{Q}_{ij}|_{\bar{s}_3=1} + r_3\nu_3\int_0^1 \bar{Q}_{ij}d\bar{s}_3 \tag{A5}$$

where

$$\left.\begin{aligned}\bar{Q}_{00} &= 2(\phi_{11}|_{\bar{s}_1=1}\chi_{113} - \chi_{111}|_{\bar{s}_1=1}\phi_{13}) \\ \bar{Q}_{01} &= 2(\phi_{11}|_{\bar{s}_1=1}\chi_{123} + \phi_{21}|_{\bar{s}_1=1}\chi_{113} \\ &\quad - \chi_{121}|_{\bar{s}_1=1}\phi_{13} - \chi_{111}|_{\bar{s}_1=1}\phi_{23}) \\ \bar{Q}_{02} &= 2(\phi_{21}|_{\bar{s}_1=1}\chi_{123} - \chi_{121}|_{\bar{s}_1=1}\phi_{23}) \\ \bar{Q}_{10} &= 2(\phi_{11}|_{\bar{s}_1=1}\chi_{123} - \chi_{121}|_{\bar{s}_1=1}\phi_{13}) \\ \bar{Q}_{11} &= 2(\phi_{11}|_{\bar{s}_1=1}\chi_{223} + \phi_{21}|_{\bar{s}_1=1}\chi_{123} \\ &\quad - \chi_{221}|_{\bar{s}_1=1}\phi_{13} - \chi_{121}|_{\bar{s}_1=1}\phi_{23}) \\ \bar{Q}_{12} &= 2(\phi_{21}|_{\bar{s}_1=1}\chi_{223} - \chi_{221}|_{\bar{s}_1=1}\phi_{23}).\end{aligned}\right\} \tag{A6}$$

Coefficients Θ_{ij} are defined as follows:

$$\Theta_{ij} = \frac{1}{2}r_3\nu_3\left(R_t\bar{\Theta}_{ij}|_{\bar{s}_3=1} + \int_0^1 \bar{\Theta}_{ij}d\bar{s}_3\right) + \frac{\gamma_t}{\nu_3^3}\bar{\bar{\Theta}}_{ij}|_{\bar{s}_3=1} \tag{A7}$$

where the values for each combination are given in (A8), shown at the bottom of the page. Coefficients K_i are defined as follows:

$$K_i = \frac{1}{2}\frac{\alpha}{\nu_3^4}\int_0^1 \bar{K}_i d\bar{s}_3 + \frac{1}{8}\frac{N}{\kappa^2(\nu_1+\nu_2)}\bar{\bar{K}}_i \tag{A9}$$

$$\left.\begin{aligned}\bar{\Theta}_{00} &= 4\,\chi_{113}^2 & \bar{\Theta}_{01} &= 8\,\chi_{113}\chi_{123} & \bar{\Theta}_{02} &= 4\,\chi_{123}^2 \\ \bar{\Theta}_{10} &= 8\,\chi_{113}\chi_{123} & \bar{\Theta}_{11} &= 8\,\chi_{123}^2 + 8\,\chi_{113}\chi_{223} & \bar{\Theta}_{12} &= 4\,\chi_{123}\chi_{223}, \\ \bar{\Theta}_{20} &= 4\,\chi_{123}^2 & \bar{\Theta}_{21} &= 8\,\chi_{123}\chi_{223} & \bar{\Theta}_{22} &= 4\,\chi_{223}^2\end{aligned}\right\}$$

$$\left.\begin{aligned}\bar{\bar{\Theta}}_{00} &= 3\,\chi'_{113}\phi'^2_{13} + \phi'^4_{13} \\ \bar{\bar{\Theta}}_{01} &= 2\,\chi'_{123}\phi'^2_{13} + 4\,\chi'_{113}\phi'_{13}\phi'_{23} + 2\,\phi'^3_{13}\phi'_{23} \\ \bar{\bar{\Theta}}_{02} &= \chi'_{113}\phi'^2_{23} + 2\,\chi'_{123}\phi'_{13}\phi'_{23} + \phi'^2_{13}\phi'^2_{23} \\ \bar{\bar{\Theta}}_{10} &= 2\,\chi'_{113}\phi'_{13}\phi'_{23} + 4\,\chi'_{123}\phi'^2_{13} + 2\,\phi'^3_{13}\phi'_{23} \\ \bar{\bar{\Theta}}_{11} &= 2\,\chi'_{223}\phi'^2_{13} + 8\,\chi'_{123}\phi'_{13}\phi'_{23} + 2\,\chi'_{113}\phi'^2_{23} + 4\,\phi'^2_{13}\phi'^2_{23} \\ \bar{\bar{\Theta}}_{12} &= 2\,\chi'_{223}\phi'_{13}\phi'_{23} + 4\,\chi'_{123}\phi'^2_{23} + 2\,\phi'_{13}\phi'^3_{23} \\ \bar{\bar{\Theta}}_{20} &= \chi'_{223}\phi'^2_{13} + 2\,\chi'_{123}\phi'_{13}\phi'_{23} + \phi'^2_{13}\phi'^2_{23} \\ \bar{\bar{\Theta}}_{21} &= 2\,\chi'_{123}\phi'^2_{23} + 4\,\chi'_{223}\phi'_{13}\phi'_{23} + 2\,\phi'_{13}\phi'^3_{23} \\ \bar{\bar{\Theta}}_{22} &= 3\,\chi'_{223}\phi'^2_{23} + \phi'^4_{23}\end{aligned}\right\} \tag{A8}$$

where

$$\left.\begin{array}{l}\bar{K}_0=\phi_{13}^{'2}\phi_{13}^{''2}\quad \bar{K}_1=2\phi_{13}^{'}\phi_{23}^{'}\phi_{13}^{''2}+2\phi_{13}^{'2}\phi_{13}^{''}\phi_{23}^{''}\\ \bar{K}_2=\phi_{23}^{'2}\phi_{13}^{''2}+4\phi_{13}^{'}\phi_{23}^{'}\phi_{13}^{''}\phi_{23}^{''}+\phi_{13}^{'2}\phi_{23}^{''2}\\ \bar{K}_3=2\phi_{13}^{'}\phi_{23}^{''2}+2\phi_{23}^{'}\phi_{13}^{''}\phi_{23}^{'}\quad \bar{K}_4=\phi_{23}^{'2}\phi_{23}^{''2}\end{array}\right\}$$
$$\left.\begin{array}{l}\bar{\bar{K}}_0=K_a^2\quad \bar{\bar{K}}_1=2K_aK_c\quad \bar{\bar{K}}_2=2K_aK_b+K_c^2\\ \bar{\bar{K}}_3=2K_bK_c\quad \bar{\bar{K}}_4=K_b^2\quad K_a=\sum_{i=1}^{2}\int_0^1\frac{\phi_{1i}^{'2}}{\nu_i}d\bar{s}_i\\ K_b=\sum_{i=1}^{2}\int_0^1\frac{\phi_{2i}^{'2}}{\nu_i}d\bar{s}_i\quad K_c=2\sum_{i=1}^{2}\int_0^1\frac{\phi_{1i}^{'}\phi_{2i}^{'}}{\nu_i}d\bar{s}_i.\end{array}\right\}\quad\text{(A10)}$$

The electrostatic potential terms f_{ij} and h_{ij} in the two-mode Lagrangian (30) are decribed as follows:

$$\left.\begin{array}{l}f_{ij}=(-1)^i\frac{(j-1)!}{i!(i-j-1)!}\Big(\frac{\nu_1}{g_1^i}\int_{1-\bar{l}_1}^1\phi_{11}^{(i+1-j)}\phi_{21}^{(j-1)}d\bar{s}_1\\ \qquad\qquad -\frac{\hat{b}_2}{\hat{b}_1}\frac{g_1}{g_2}\frac{\nu_2}{g_2^i}\int_{1-\bar{l}_2}^1\phi_{12}^{(i+1-j)}\phi_{22}^{(j-1)}d\bar{s}_2\Big)\\ h_{ij}=(-1)^i\frac{(j-1)!}{i!(i-j-1)!}\Big(\frac{\hat{b}_3}{\hat{b}_1}\frac{g_1}{g_3}\frac{\nu_3}{g_3^i}\int_{1-\bar{l}_3}^1\phi_{13}^{(i+1-j)}\phi_{23}^{(j-1)}d\bar{s}_3\Big).\end{array}\right\}\quad\text{(A11)}$$

The parameters η_{ij} in the equations of motion in (36) are given as follows:

$$\left.\begin{array}{l}\eta_{12}=\frac{1}{2\Gamma_{11}|_{\epsilon=0}}\Big(-\omega_2^2\left(2\frac{\partial\Gamma_{12}}{\partial\epsilon}+Q_{01}\bar{A}_{10}+Q_{11}\bar{A}_{20}\right)\\ \qquad\qquad +\Big(2\frac{\partial W_{12}}{\partial\epsilon}-f_{22}\hat{F}_{01}-h_{22}\hat{F}_{02}\Big)\Big)\\ \eta_{21}=\frac{1}{2\Gamma_{22}|_{\epsilon=0}}\Big(-\omega_1^2\left(2\frac{\partial\Gamma_{12}}{\partial\epsilon}+Q_{01}\bar{A}_{10}+Q_{11}\bar{A}_{20}\right)\\ \qquad\qquad +\Big(2\frac{\partial W_{12}}{\partial\epsilon}-f_{22}\hat{F}_{01}-h_{22}\hat{F}_{02}\Big)\Big)\\ \eta_{13}=-\frac{1}{\Gamma_{11}|_{\epsilon=0}}\omega_1^2Q_{00}\\ \eta_{14}=-\frac{1}{2\Gamma_{11}|_{\epsilon=0}}\omega_2^2Q_{11}\\ \eta_{15}=-\frac{1}{2\Gamma_{11}|_{\epsilon=0}}\left(\omega_2^2Q_{01}+2\omega_1^2Q_{10}\right)\\ \eta_{16}=-\frac{1}{2\Gamma_{11}|_{\epsilon=0}}Q_{00}\\ \eta_{17}=\frac{1}{2\Gamma_{11}|_{\epsilon=0}}(Q_{11}-Q_{02})\\ \eta_{18}=\frac{Q_{10}}{\Gamma_{11}|_{\epsilon=0}}\\ \eta_{23}=-\frac{1}{2\Gamma_{22}|_{\epsilon=0}}\omega_1^2Q_{01}\\ \eta_{24}=-\frac{1}{\Gamma_{22}|_{\epsilon=0}}\omega_2^2Q_{12}\\ \eta_{25}=-\frac{1}{2\Gamma_{22}|_{\epsilon=0}}\left(\omega_1^2Q_{11}+2\omega_2^2Q_{02}\right)\\ \eta_{26}=\frac{1}{2\Gamma_{22}|_{\epsilon=0}}(Q_{01}-Q_{10})\\ \eta_{27}=\frac{1}{2\Gamma_{22}|_{\epsilon=0}}Q_{12}\\ \eta_{28}=\frac{Q_{02}}{\Gamma_{22}|_{\epsilon=0}}.\end{array}\right\}\quad\text{(A12)}$$

REFERENCES

[1] A. P. Davila, J. Jang, A. K. Gupta, T. Walter, A. Aronson, and R. Bashir, "Microresonator mass sensors for detection of *Bacillus anthracis* sterne spores in air and water," *Biosens. Bioelectron.*, vol. 22, no. 12, pp. 3028–3035, Jun. 2007.

[2] A. Gupta, D. Akin, and R. Bashir, "Single virus particle mass detection using microresonators with nanoscale thickness," *Appl. Phys. Lett.*, vol. 84, no. 11, pp. 1976–1978, Mar. 2004.

[3] B. Ilic, D. Czaplewski, and H. G. Craighead, "Mechanical resonant immunospecific biological detector," *Appl. Phys. Lett.*, vol. 77, no. 3, pp. 450–452, Jul. 2000.

[4] A. Zribi, A. Knobloch, W.-C. Tian, and S. Goodwin, "Micromachined resonant multiple gas sensor," *Sens. Actuators A, Phys.*, vol. 122, no. 1, pp. 31–38, Jul. 2005.

[5] C. J. Welham, J. W. Gardner, and J. Greenwood, "A laterally driven micromachined resonant pressure sensor," *Sens. Actuators A, Phys.*, vol. 52, no. 1–3, pp. 86–91, Mar./Apr. 1996.

[6] A. A. Seshia, M. Palaniapan, T. A. Roessig, R. T. Howe, R. W. Gooch, T. R. Schimert, and S. Montague, "A vacuum packaged surface micromachined resonant accelerometer," *J. Microelectromech. Syst.*, vol. 11, no. 6, pp. 784–793, Dec. 2002.

[7] N. Yazdi, F. Ayazi, and K. Najafi, "Micromachined inertial sensors," *Proc. IEEE*, vol. 86, no. 8, pp. 1640–1659, Aug. 1998.

[8] C. Acar and A. M. Shkel, "Structurally decoupled micromachined gyroscopes with post-release capacitance enhancement," *J. Micromech. Microeng.*, vol. 15, no. 5, pp. 1092–1101, May 2005.

[9] J. R. Clark, W.-T. Hsu, M. A. Abdelmoneum, and C. T.-C. Nguyen, "High-q UHF micromechanical radial-contour mode disk resonators," *J. Microelectromech. Syst.*, vol. 14, no. 6, pp. 1298–1310, Dec. 2005.

[10] C. T.-C. Nguyen, "Vibrating RF MEMS for next generation wireless applications," in *Proc. Custom Integr. Circuits Conf.*, Orlando, FL, Oct. 3–6, 2004, pp. 257–264.

[11] K. Wang, A.-C. Wong, and C. T.-C. Nguyen, "VHF free–free beam high-q micromechanical resonators," *J. Microelectromech. Syst.*, vol. 9, no. 3, pp. 347–360, Sep. 2000.

[12] S. Hu and A. Raman, "Chaos in atomic force microscopy," *Phys. Rev. Lett.*, vol. 96, no. 3, p. 036 107, Jan. 2006.

[13] Q. Huang, S. Gonda, I. Misumia, O. Sato, T. Keema, and T. Kurosawa, "Nonlinear and hysteretic influence of piezoelectric actuators in AFMs on lateral dimension measurement," *Sens. Actuators A, Phys.*, vol. 125, no. 2, pp. 590–596, Jan. 2006.

[14] M. I. Younis and A. H. Nayfeh, "A study of the nonlinear response of a resonant microbeam to an electric actuation," *Nonlinear Dyn.*, vol. 31, no. 1, pp. 91–117, Jan. 2003.

[15] S. K. De and N. R. Aluru, "Complex nonlinear oscillations in electrostatically actuated microstructures," *J. Microelectromech. Syst.*, vol. 15, no. 2, pp. 355–369, Apr. 2006.

[16] I. Kozinsky, H. W. C. Postma, I. Bargatin, and M. L. Roukes, "Tuning nonlinearity, dynamic range, and frequency of nanomechanical resonators," *Appl. Phys. Lett.*, vol. 88, no. 25, p. 253 101, Jun. 2006.

[17] R. Baskaran and K. L. Turner, "Mechanical domain coupled mode parametric resonance and amplification in a torsional mode micro electro mechanical oscillator," *J. Micromech. Microeng.*, vol. 13, no. 5, pp. 701–707, Sep. 2003.

[18] K. L. Turner, S. A. Miller, P. G. Hartwell, N. C. MacDonald, S. H. Strogatz, and S. G. Adams, "Five parametric resonances in a microelectromechanical system," *Nature*, vol. 396, no. 6707, pp. 149–152, Nov. 1998.

[19] A. H. Nayfeh, *Nonlinear Interactions: Analytical, Computational and Experimental Methods*. New York: Wiley Interscience, 2000.

[20] W. Zhang and K. L. Turner, "Application of parametric resonance amplification in a single-crystal silicon micro-oscillator based mass sensor," *Sens. Actuators A, Phys.*, vol. 122, no. 1, pp. 23–30, Jul. 2005.

[21] J. F. Rhoads, S. W. Shaw, K. L. Turner, and R. Baskaran, "Tunable microelectromechanical filters that exploit parametric resonance," *J. Vib. Acoust.*, vol. 127, no. 5, pp. 423–430, Oct. 2005.

[22] A. Vyas and A. K. Bajaj, "Dynamics of autoparametric vibration absorbers using multiple pendulums," *J. Sound Vib.*, vol. 246, no. 1, pp. 115–135, Sep. 2001.

[23] A. Bajaj, S. Chang, and J. Johnson, "Amplitude modulated dynamics of a resonantly excited autoparametric two degree-of-freedom system," *Nonlinear Dyn.*, vol. 5, no. 4, pp. 433–457, Jun. 1994.

[24] B. Balachandran and A. H. Nayfeh, "Nonlinear motions of a beam-mass structure," *Nonlinear Dyn.*, vol. 1, no. 1, pp. 39–61, Jan. 1990.

[25] R. S. Haxton and A. D. S. Barr, "The autoparametric vibration absorber," *Trans. ASME, J. Eng. Ind.*, vol. 94, pp. 119–225, 1972.

[26] A. H. Nayfeh and D. T. Mook, *Nonlinear Oscillations*. New York: Wiley Interscience, 1979.

[27] S. Pamidighantam, R. Puers, K. Baert, and H. Tilmans, "Pull-in voltage analysis of electrostatically actuated beam structures with fixed–fixed and fixed–free end conditions," *J. Micromech. Microeng.*, vol. 12, no. 4, pp. 458–464, Jul. 2002.

[28] G. M. Rabeiz, *RF MEMS: Theory, Design, and Technology*. Hoboken, NJ: Wiley, 2003.

[29] A. H. Nayfeh and P. F. Pai, *Linear and Nonlinear Structural Mechanics*. Hoboken, NJ: Wiley Interscience, 2002.

[30] L. Meirovitch, *Principles and Techniques of Vibrations*. Upper Saddle River, NJ: Prentice-Hall, 1997.

[31] J. A. Pelesko and D. H. Bernstein, *Modeling MEMS and NEMS*. Boca Raton, FL: CRC Press, 2003.
[32] J. A. Murdock, *Perturbations: Theory and Methods*. New York: Wiley, 1991.
[33] A. H. Nayfeh, M. I. Younis, and E. Abdel-Rahman, "Dynamic pull-in phenomenon in MEMS resonators," *Nonlinear Dyn.*, vol. 48, no. 1/2, pp. 153–163, Apr. 2007.
[34] H. A. C. Tilmans, W. D. Raedt, and E. Beyne, "MEMS for wireless communications: 'From RF-MEMS components to RF-MEMS-sip'," *J. Micromech. Microeng.*, vol. 13, no. 4, pp. S139–S163, Jul. 2003.
[35] E. Doedel, "AUTO: Software for continuation and bifurcation problems in ordinary differential equations," Dept. Appl. Math., California Inst. Technol., Pasadena, CA, Rep. 1986.
[36] K. Ekinci, M. Huang, and M. Roukes, "Ultrasensitive nanoelectromechanical mass detection," *Appl. Phys. Lett.*, vol. 84, no. 22, pp. 4469–4471, May 2004.
[37] B. Ilic, H. Craighead, S. Krylov, W. Senaratne, C. Ober, and P. Neuzil, "Attogram detection using nanoelectromechanical oscillators," *J. Appl. Phys.*, vol. 95, no. 7, pp. 3694–3703, Apr. 2004.
[38] M. Madou, *Fundamentals of Microfabrication*. Boca Raton, FL: CRC Press, 1997.
[39] MEMSCAP Inc., *PolyMUMPS Run Data for Run No. 61 to 81*, 2008. [Online]. Available: http://www.memscap.com/mumps/nc-pmumps.refs.html
[40] A. Vyas, "Microresonator designs based on nonlinear 1 : 2 internal resonance between flexural–flexural and torsional–flexural structural modes," Ph.D. dissertation, Purdue Univ., West Lafayette, IN, 2008.

Ashwin Vyas received the B.Tech. degree in mechanical engineering from the Indian Institute of Technology, Guwahati, India, in 1999, and the M.S. and Ph.D. degrees in mechanical engineering from Purdue University, West Lafayette, IN, in 2001 and 2008, respectively. His thesis included work on the design and analysis of nonlinear microresonator devices.

He is currently working as a Senior Controls Engineer with Cummins Inc., Columbus, IN.

Dr. Vyas is a Student Member of the American Society of Mechanical Engineers.

Dimitrios Peroulis (S'99–M'04) received the Diploma degree in electrical and computer engineering from the National Technical University of Athens, Athens, Greece, in 1998, and the M.S.E.E. and Ph.D. degrees in electrical engineering from The University of Michigan, Ann Arbor, in 1999 and 2003, respectively.

Since August 2003, he has been an Assistant Professor with the School of Electrical and Computer Engineering, Purdue University, West Lafayette, IN. His research work is focused on microelectromechanical systems (MEMS) for multifunctional communications systems and sensors. His group is currently part of two research centers funded by DARPA (IMPACT center) and the National Nuclear Security Administration (PRISM center) that are focused on MEMS failure mechanisms and reliability.

Anil K. Bajaj received the B.S. degree in mechanical engineering from the Indian Institute of Technology, Kharagpur, India, the M.S. degree in mechanical engineering from the Indian Institute of Technology, Kanpur, India, and the Ph.D. degree in mechanics from the University of Minnesota.

In January 1981, he joined Purdue University, West Lafayette, IN, where, since 1991, he has been a Professor with the School of Mechanical Engineering. His research and teaching interests include the areas of linear and nonlinear systems, analytical dynamics and modeling of multibody systems, stability of elastic systems, dynamics of robotic systems, bifurcations and chaos in mechanical systems, and nonlinear stability in fluids and fluid–structure interaction problems. Specifically, he is interested in modeling and design of nonlinear resonant MEMS and in modeling and dynamics of seat-occupant systems in vehicles.